Journal of
Materials Chemistry A

REVIEW

View Article Online
View Journal | View Issue

Check for updates

Cite this: *J. Mater. Chem. A*, 2022, **10**, 19231

Manganese-based layered oxides for electrochemical energy storage: a review of degradation mechanisms and engineering strategies at the atomic level

Shuo Sun,†[a] Jin Li,†[a] Cuixia Xu,[b] Teng Zhai *[a] and Hui Xia*[a]

The ever-increasing demand for high-energy-density electrochemical energy storage has been driving research on the electrochemical degradation mechanisms of high-energy cathodes, among which manganese-based layered oxide (MLO) cathodes have attracted high attention thanks to their low cost and eco-friendliness. More importantly, MLO materials with large and tunable interlayer spacing are ideal candidates for the insertion of (monovalent, divalent, trivalent) alkaline ions, such as Li^+, Na^+, K^+, Zn^{2+}, Mg^{2+}, and Al^{3+}, enabling impressive electrochemical performance. Nevertheless, the local MnO_6 octahedron distortion induced by the Jahn–Teller (J–T) effect can lead to irreversible phase transformation, dissolution/disproportionation reactions, interfacial degradation arising from Mn^{2+}, and crack formation, which significantly impact the electrochemical stability of MLO materials. Hence, in this review, we discuss the various degradation processes caused by J–T distortion in MLO cathodes at the atomic level. Advances in the atomic-level structure and property optimizations of MLO materials and in-depth structure–function–property correlations are also systematically reviewed. Finally, we provide our perspectives on the future development of MLO materials. The integration of high-performance MLO cathodes in energy storage devices has great potential to address growing global energy demands.

Received 21st March 2022
Accepted 17th May 2022

DOI: 10.1039/d2ta02242g

rsc.li/materials-a

1. Introduction

Triggered by the overuse of traditional nonrenewable energy supplies, energy crisis and climate change have become serious global issues.[1,2] In this regard, it is of particular importance to transit from fossil fuels towards clean and sustainable energy sources (especially wind and solar energy). Thus, developing low-cost, environmentally friendly, and highly efficient energy storage techniques is crucial for storing and utilizing these

---

[a] Herbert Gleiter Institute of Nanoscience, School of Materials Science and Engineering, Nanjing University of Science and Technology, Nanjing, Jiangsu Province, China. E-mail: tengzhai@njust.edu.cn; xiahui@njust.edu.cn

[b] Jiangsu Key Laboratory for Biofunctional Molecules, College of Life Science and Chemistry, Jiangsu Second Normal University, Nanjing 210013, P. R. China

† These authors contributed equally to this work.

Shuo Sun received his B.E. degree (2015) at the Xuzhou Institute of Technology and M.S. degree at Nanjing University of Science and Technology (2015). He obtained his PhD degree at Nanjing University of Science and Technology in 2021. Then he joined Tsinghua University in 2021 and his research interests focus on the design of interface electrochemistry of cathodes in aqueous energy storage and all-solid-state lithium metal batteries.

Jin Li received his B.E. degree (2019) at Jiangsu University. He is currently pursuing his PhD degree at the School of Materials Science and Engineering, Nanjing University of Science and Technology. His research interests focus on the regulation of the surface/interface in aqueous batteries.

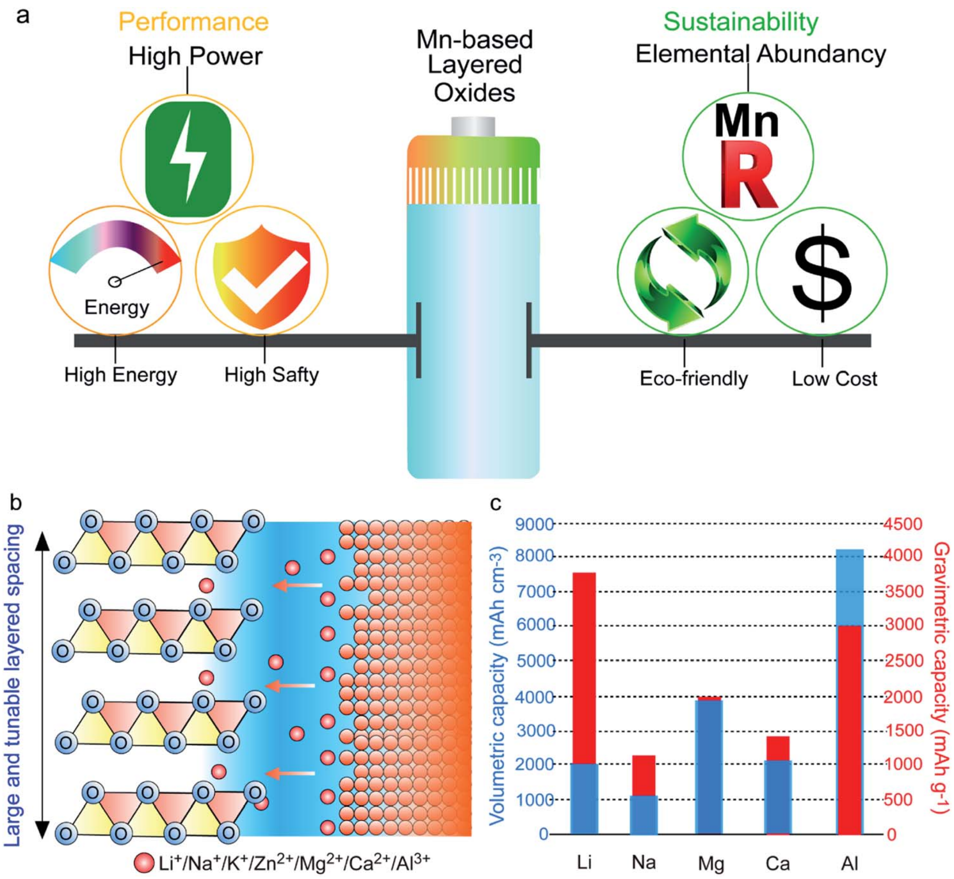

Fig. 1 (a) Schematic illustrations of the balance between the electrochemical performance and sustainability in MLO materials. (b) MLO materials with large and tunable layered spacing enabling the insertion of various valence ions. (c) Volumetric capacity and gravimetric capacity for the various metal anodes.

intermittent sustainable energies for the following utilization, which can address the energy crisis, reduce CO_2 emissions, and contribute to achieving a more sustainable society.[3,4] Particular interest has been directed towards electrochemical energy storage systems, such as supercapacitors, Li-ion batteries, Na-ion batteries, Zn-ion batteries, and Al-based batteries, which are regarded as the most promising technologies to meet the skyrocketing energy consumption demands of consumer

Teng Zhai is currently a professor at the School of Materials Science and Engineering, Nanjing University of Science and Technology (NJUST, China). Prior to joining NJUST in 2015, he received his PhD degree at Sun Yat-Sen University (China). He was a visiting scholar at the University of California, Santa Cruz (UCSC, USA) from 2013 to 2015. His research interest focuses on the surface/interface modification of nanomaterials for energy storage systems, such as supercapacitors, aqueous batteries, and metal-iodine batteries.

Hui Xia is a full professor at the School of Materials Science and Engineering, Nanjing University of Science and Technology. He received his B.E. and M.S. degrees from the University of Science and Technology Beijing in 2000 and 2003, and completed his PhD degree from the National University of Singapore in 2007. From 2007 to 2011, he was a research fellow at the National University of Singapore. Prof. Xia joined Nanjing University of Science and Technology in 2011 and his research interests focus on electrode materials and architectures for all-solid-state thin-film micro-batteries, Li^+/Na^+ ion batteries, supercapacitors, and new energy storage systems.

electronics, electric vehicles, and large-scale energy storage devices.[5–10] Electrochemical energy storage involves the conversion of chemical energy into electrical energy *via* ion shift between the cathode side and the anode side. Therefore, designing high-performance electrodes is crucial for advancing energy storage solutions. In the endeavors to improve energy storage technologies, the high-performance cathode material is the main bottleneck.

Among the various cathode candidates, transition metal (TM) layered oxides provide many advantages thanks to their high capacities, simple structures, and ease of synthesis.[11–13] Although different TMs, including Ni, Co, and Mn, have been utilized in layered cathode materials, only Mn-based layered cathode materials realize the ideal balance between sustainability and performance (Fig. 1a). Mn has the highest crust abundance among Ni, Co, and Mn (84 ppm, 25 ppm, and 950 ppm, respectively)[14] and thus the lowest costs. Additionally, elemental Mn is nontoxic and eco-friendly, and the risks of metal pollution with Mn use are lower than those of Ni and Co.[8,15,16] In terms of performance, owing to the high redox activity of $Mn^{2+}/Mn^{3+}/Mn^{4+}$ and the corresponding high redox potential, as well as the relatively low atomic weight, Mn-based layered oxides (MLOs) deliver much higher energy densities than other cathode materials.[4,14] Meanwhile, unlike Ni-based layered oxides, MLOs possess high thermal stability and are thus safer.[17] Furthermore, the large and tunable interlayer spacing of MLO materials guarantees fast ionic diffusion kinetics, providing an ideal structure for (monovalent, divalent, trivalent) alkaline ions (*e.g.*, Li^+, Na^+, K^+, Zn^{2+}, Mg^{2+}, Ca^{2+}, Al^{3+}) insertion, representing a star family as cathode materials in various electrochemical energy storage devices for a long period (Fig. 1b).[18–20] Apart from the commonly used metal anodes, such as Li, Na, and K, metal anode materials like Zn, Mg, and Al, which boast the merits of earth abundance, safety, good machinability, and ultrahigh volumetric energy density, are also attractive candidates for energy storage. Therefore, the development of MLO cathodes is beneficial to develop advanced energy storage devices and satisfy the future demands of large-scale energy storage.

The typical MLO materials are built by alternately layering TM–oxygen and alkaline metal ions. The TM is coordinated in an octahedral geometry by oxygen, and the alkaline metal ions are inserted in prismatic (P), tetrahedral (T), and octahedral (O) configurations, corresponding to the P2/P3, T2, and O2/O3 phases, respectively (Fig. 2a), in which the numbers 2 and 3 represent the repeat period of the TM–O layers.[21,22] In addition,

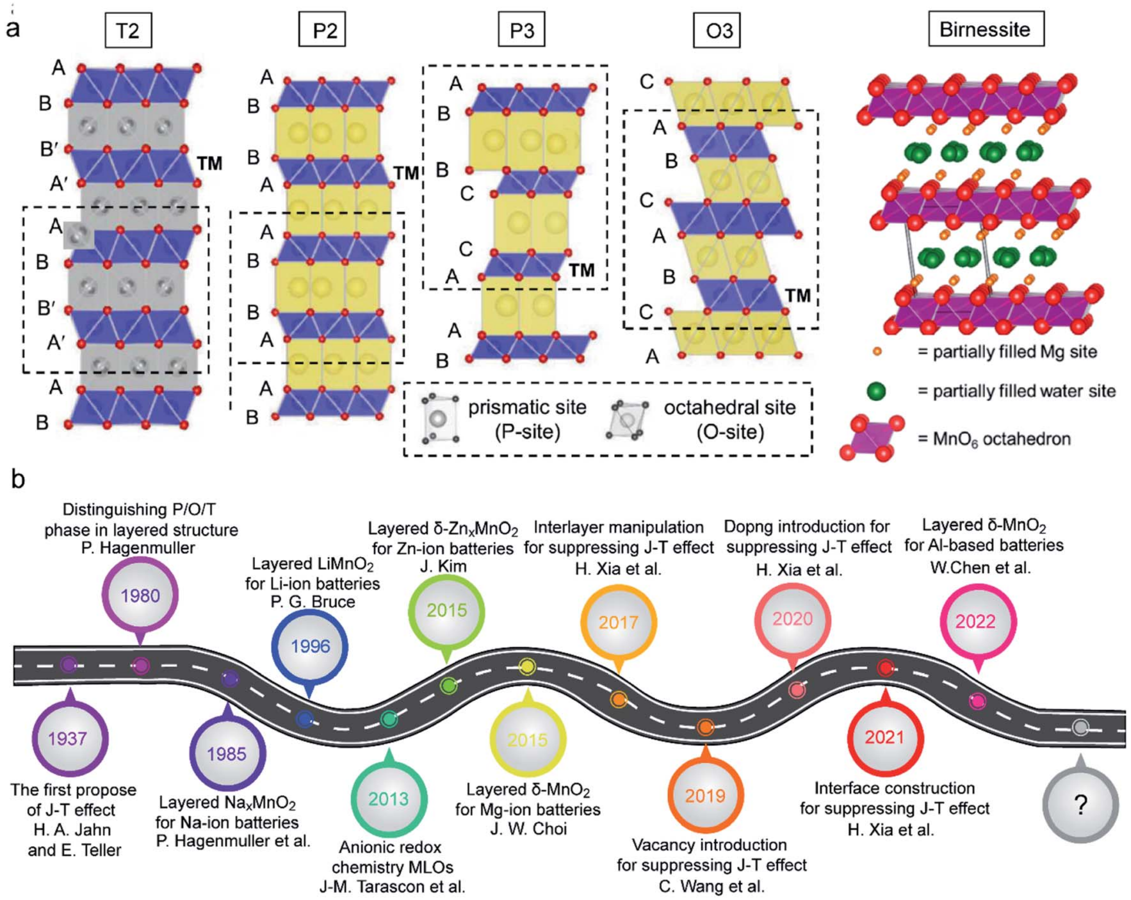

Fig. 2 (a) Schematic illustrations of the crystal structures of the birnessite phase, reproduced with permission.[31] Copyright 2015 American Chemical Society. Schematic illustrations of T, P, and O phases. Reproduced with permission.[22] Copyright 2021 Wiley-VCH. (b) Main progress of MLOs in various energy storage systems, including Li, Na, K, Zn, Al, *etc.* batteries, as well as supercapacitors.

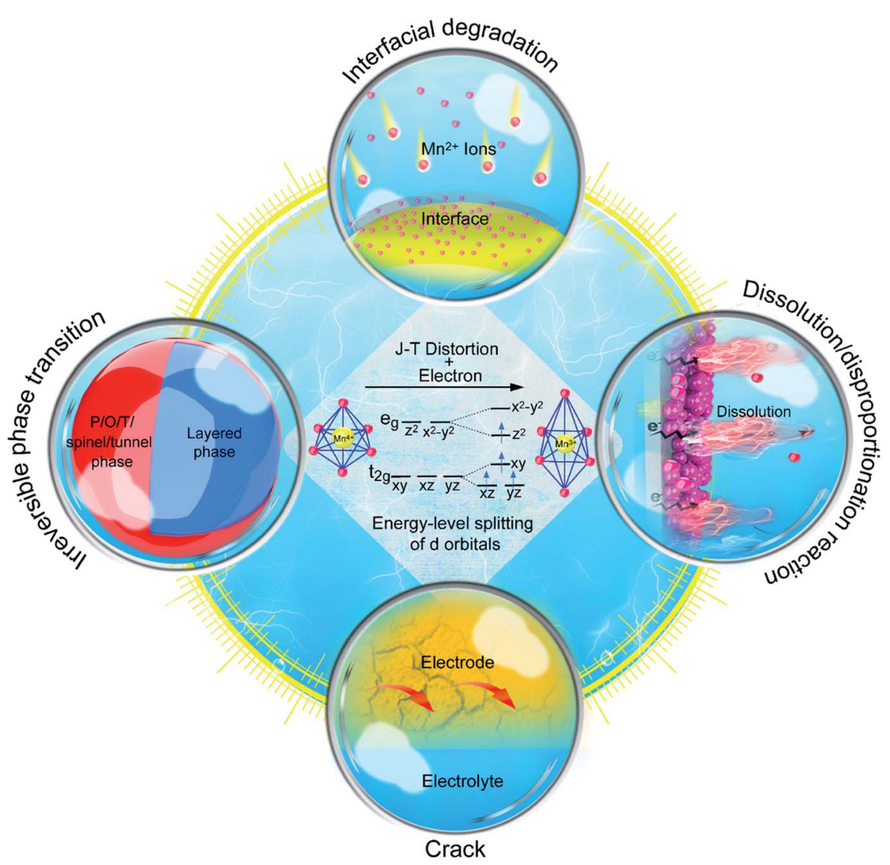

Fig. 3 The main electrochemical degradation mechanisms induced by J–T distortion in MLO cathodes.

a special kind of MLO material, called birnessite, comprises a mixed-valent oxide surrounded by six oxygen atoms to constitute a basic unit [MnO_6] octahedron with cations of various valences (*e.g.*, K^+, Na^+, Zn^{2+}) and crystal water filling the interlayers.[23,24] Birnessite, with 2D interlayer space for ionic diffusion, is a hydrous Mn oxide. Layered oxides were first applied in energy storage by J. B. Goodenough in 1980;[25] substantial efforts have since advanced the development of high-performance MLO materials for various energy storage purposes (Fig. 2b).[26–30] Although remarkable progress has been made, the applications of MLO materials are still limited by irreversible phase transition, Mn dissolution/disproportionation reactions, interfacial degradation arising from Mn^{2+}, and crack formation (Fig. 3), which lead to rapid electrochemical degradation. It is worth noting that the root of these detrimental issues is local MnO_6 octahedron distortion caused by the Jahn–Teller (J–T) effect. The J–T theorem was proposed by H.A. Jahn and E. Teller in 1937;[32] due to this effect, a nonlinear molecular system suffers from instability in the degenerate electron state. Mn has several oxidation states (+2, +3, +4, +7), and electrochemical redox reactions usually happen between the +4 and +2 oxidation states. The ligand field of Mn^{4+} is shown at the center of Fig. 3. The Mn ions are coordinated by six oxide ligands and are symmetrically arranged along the Cartesian axes. The electric field of the octahedrally arranged ligands separates the d orbitals of Mn into doubly degenerate e_g (d_{z^2} and $d_{x^2-y^2}$) and triply degenerate t_{2g} (d_{xy}, d_{xz}, and d_{yz}) sets. The e_g orbital set of Mn^{4+} is empty, thus possessing a cubically symmetrical electron density. This feature confers stability to Mn^{4+}-derived layered materials. However, when Mn^{3+} is coordinated with oxygen, like in $LiMnO_2$, the $3d^4$ configuration of Mn^{3+} exhibits an asymmetrical electron density distribution and a high-spin state due to the single-electron occupancy in the e_g level.[33–35] In this case, the two axial Mn–O bonds are elongated and the four equatorial bonds are shortened to relax this unfavorable state, *i.e.*, the J–T distortion, transforming MnO_6 from the cubic configuration into the tetragonal configuration. As such, this structural evolution at the atomic level detrimentally impacts the physicochemical properties of MLO materials.

In attempts to prevent J–T distortion, various strategies have been developed to optimize structural stability at the atomic level during the charging/discharging process.[7,34,36–40] These strategies can be divided into four categories (Fig. 3): (i) elemental doping, (ii) interlayered structure manipulation, (iii) vacancy introduction, and (iv) novel structural design. Although previous reviews have discussed Mn-based and/or layered cathode materials, the relationships between the structural evolution of MLO materials at the atomic level and capacity fade during the ion deintercalation/intercalation processes have not been systematically reviewed.[12,41–43] In particular, a comprehensive review of the atomic-level mechanisms and strategies that remedy the electrochemical degradation of MLO cathodes in various valence ion-based electrochemical energy storage devices is needed.

In this review, we discuss the relationships between the intrinsic structure, electrochemical behaviors, and degradation mechanisms from the perspective of the atomic level and summarize the effective strategies for structural degradation during ion deintercalation/intercalation. We begin by discussing the different electrochemical behaviors resulting from alkaline ion insertion into MLO cathodes, from monovalent ions to trivalent ions. Moreover, we describe the corresponding electrochemical degradation caused by irreversible phase transition, Mn dissolution/disproportionation reactions, interfacial degradation arising from Mn^{2+}, and crack formation in various energy storage devices, as well as the relationships between these degradation mechanisms and J–T distortion. Finally, we outline the recent achievements in overcoming the aforementioned bottlenecks and provide perspectives on the future development of high-performance MLO materials.

2. Fundamental understanding of alkaline ion insertion in MLO materials

Energy storage devices based on multivalent metal ions with high crust abundances, such as Ca, Mg, Zn, and Al, have the potential to satisfy the future demands of large-scale energy storage. Therefore, as an alternative to the development of conventional monovalent metal energy storage (*e.g.*, Li batteries, Na batteries), divalent and trivalent ion intercalation is of particular importance. Nevertheless, unlike monovalent ions, the intercalation of divalent/trivalent ions into electrode materials is difficult due to the strong electrostatic interactions between the electrode material atoms and the highly charged intercalation ions. Diffusion channels that allow ion mobility are crucial to enable multivalent ion insertion. Notably, the large and tunable interlayer spacing of MLOs can accommodate structural deformations, enabling the reversible insertion of both monovalent ions and multivalent ions into MLO materials. Layered MLO structures possess 2D diffusion channels, providing a favorable structure for ionic diffusion and guaranteeing fast kinetics. The MLO materials with different structures used in various energy storage systems are summarized in Table 1, in which MLO materials exhibit superior performance due to their large and tunable interlayered spacing. In the next sections, we discuss the insertion of monovalent, divalent, and trivalent ions in MLO cathodes.

2.1 Monovalent ion insertion in MLO materials

The weak interactions between the inserted monovalent ions and atoms in the MLO structure enable fast kinetics and high electrochemical performance; Li^+, K^+, and Na^+ insertion in various MLO cathodes has been comprehensively examined. The interlayers of birnessite are filled by alkaline monovalent cations and crystal water.[23,24] Such a material is configured as an edge-sharing $[MnO_6]$ octahedron, separated by a complex interlayer environment comprising a single layer of H_2O and cations in two similar sites. The interlayer spacing is often approximately 7.0 Å but can increase to ~10.0 Å with further hydration and decrease to ~5.5 Å upon dehydration.[54] Moreover, the valence state of Mn is not completely Mn^{4+}, and the average valence is usually between 3.6 and 3.8, indicating the presence of some Mn^{3+} in the birnessite structure. Therefore, the physicochemical properties of birnessite can be altered by modulating the layer spacing, the interlayer water content, and the species of intercalated cations. Birnessite is often used for aqueous energy storage. In neutral pH electrolytes, birnessite δ-MnO_2 shows linear galvanostatic charge–discharge curves and rectangular cyclic voltammograms (CVs). This electrochemical behavior has been described as non-faradaic electrical double layer formation due to the nonspecific adsorption of partially solvated or desolvated ions.[59] Nevertheless, experimental results have demonstrated that the electrochemical behavior of δ-MnO_2 matched with monovalent ions is associated with

Table 1 Classification of manganese-based layered oxides

Energy storage type	Material	Crystal structure	Interlayer space (Å)	Electrolyte type	Rate performance	Ref.
Supercapacitor	δ-MnO_2	Birnessite	7.2	Aqueous	250 F g^{-1} at 0.2 A g^{-1} 125 F g^{-1} at 10.0 A g^{-1}	19
Li-ion battery	$LiMnO_2$	O3	5.4	Organic	286 mA h g^{-1} at 1C 183 mA h g^{-1} at 12C	44
Li-ion battery	$Li_{2/3}[Ni_{1/3}Mn_{2/3}]O_2$	T2	5.0	Organic	180 mA h g^{-1} at 0.1C	45
Li-ion battery	Li_2MnO_3	O2	4.7	Organic	400 mA h g^{-1} at 0.01 A g^{-1}	46
Na-ion battery	$NaMnO_{2-y-\delta}(OH)_{2y}$	Birnessite	7.2	Organic	211 mA h g^{-1} at 0.2C 156 mA h g^{-1} at 50C	47
Na-ion battery	Na_xMnO_2	O3 ($x = 0.9$–1.0) P2 ($x = 0.6$–0.8)	5.7	Organic	185 mA h g^{-1} at 0.1C 194 mA h g^{-1} at C/30	48
K-ion battery	$K_{0.77}MnO_2$	Birnessite	7.2	Organic	77 mA h g^{-1} at 1 A g^{-1}	24
Zn-ion battery	Zn–MnO_2	Birnessite	9.2	Aqueous	242 mA h g^{-1} at 3 A g^{-1}	49
Ca-ion battery	$CaMnO_2$	Birnessite	6.9	Aqueous	89 mA h g^{-1} at 2 A g^{-1}	50
Mg-ion battery	$MgMnO_2$	Birnessite	6.7	Aqueous	55 mA h g^{-1} at 8 A g^{-1}	51
Mg-ion battery	MnO_2	Birnessite	9.7	Aqueous	110 mA h g^{-1} at 1C 50 mA h g^{-1} at 10C	52
Al-ion battery	MnO_2	Birnessite	7.0	Aqueous	59 mA h g^{-1} at 0.1 A g^{-1}	53

pseudocapacitance, Mn oxidation state changes, local bonding, and structure.[18] In the charge/discharge process, the monovalent cations in the electrolytes, such as Na^+ and K^+, can be intercalated/deintercalated into the layered space of δ-MnO_2.[60] However, unlike the intercalation of other cations, the integration and confinement of structural water within the interlayers of δ-MnO_2 leads to electrochemical behaviors between faradaic and traditional capacitive non-faradaic electrical double layer intercalation (Fig. 4a).[19,61,62] These confined water molecules in the interlayers weaken the interactions between the intercalated ions and MnO_2 layers, resulting in minimal structural change and potential dependence (manifested as rectangular CV curves). Boyd *et al.*[19] performed electrochemical quartz crystal microbalance experiments (EQCM) and discovered that the alkali cation and H_2O intercalation into δ-MnO_2 simultaneously proceeded during the electrochemical process. In sharp contrast, the CV curves of δ-MnO_2 materials with no water showed well-defined peaks originating from the structural transitions. When H_2O molecules entered the interlayers, the CV curves became featureless, and the corresponding X-ray diffraction pattern showed only a small change in the interlayer spacing during intercalation/deintercalation.

As for the P/O/T phases, such as layered Li_xMnO_2 and Na_xMnO_2, both consist of edge-sharing MnO_6 octahedra separated by an interlayer of Li^+ or Na^+. Generally, most AMO_2 (A = Li, Na; M = transition metal) phases have α-$NaFeO_2$-type structures.[63,64] However, when M is Mn^{3+}, the crystal structure is monoclinic (space group *C*2/*m*), not orthorhombic, due to the

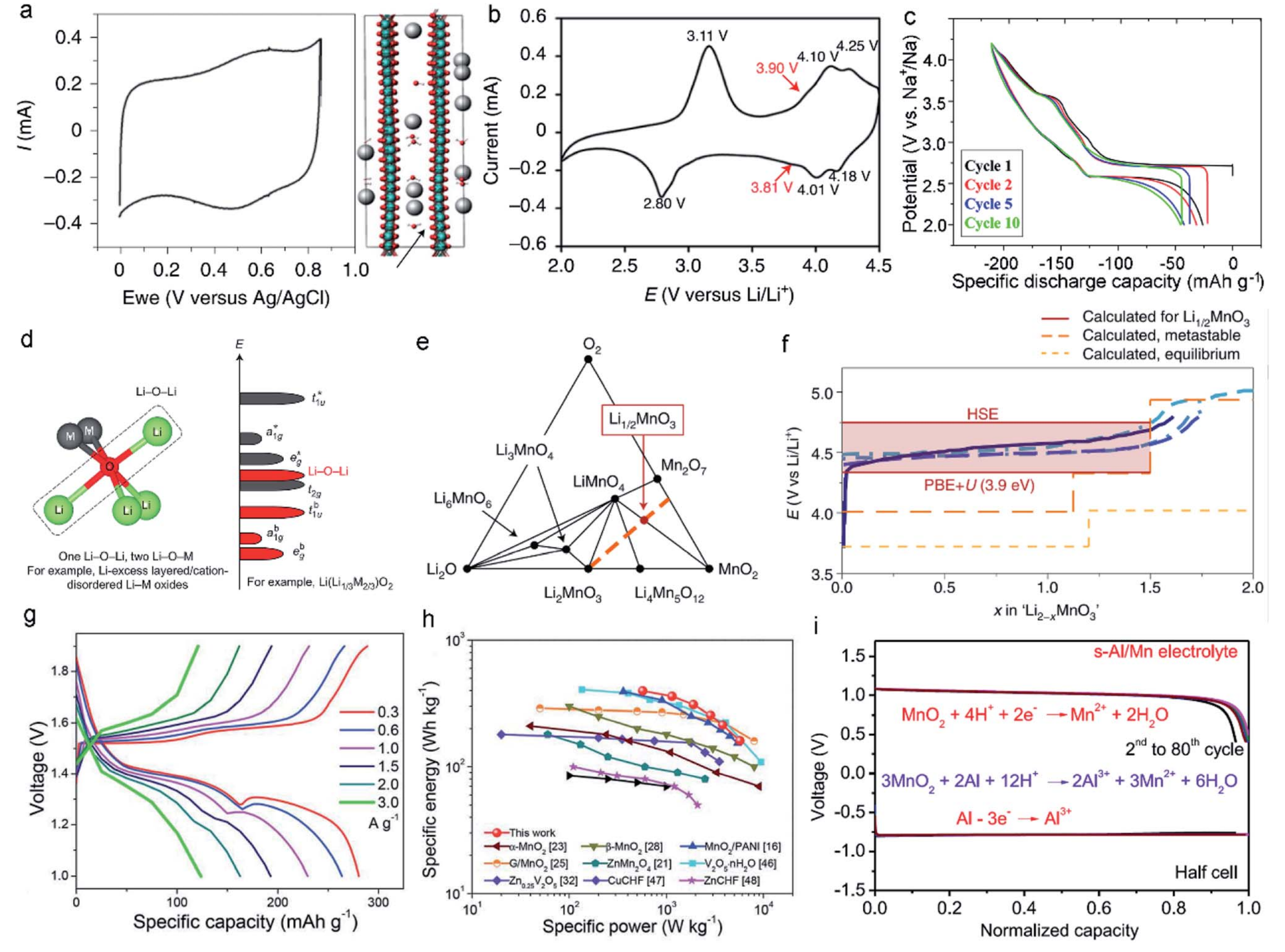

Fig. 4 (a) The typical CV of δ-MnO_2 showing nearly capacitive behavior at 10 mV s^{-1} and simulation of H_2O and K^+ intercalation into δ-MnO_2. Reproduced with permission.[19] Copyright 2021 Springer Nature. (b) CV curve of the spinel–layered $LiMnO_2$ cathode at 0.1 mV s^{-1}. Reproduced with permission.[44] Copyright 2021 Springer Nature. (c) Discharge curves of $NaMnO_2$ at a rate of 10 mA g^{-1}. The 1st, 2nd, 5th, and 10th cycles are represented by the curves with black, red, blue, and green, respectively. Reproduced with permission.[55] Copyright 2014 American Chemical Society. (d) Local atomic coordination around O with two Li–O–M and one Li–O–Li configurations in Li-excess layered oxides. Reproduced with permission.[56] Copyright 2016 Springer Nature. (e) The metastable phase diagram suggests that the Mn would be oxidized to the +7 state in the form of Mn_2O_7 and $LiMnO_4$ when the formation kinetics of oxygen–oxygen bonds is sluggish. (f) Comparison between the voltage curves for the Li_2MnO_3 component of composites and Li_2MnO_3. Reproduced with permission.[57] Copyright 2019 Springer Nature. (g) Charge/discharge curves at different current densities in ZIBs. (h) Ragone plot of ZIB-based layered MnO_2. Reproduced with permission.[58] Copyright 2019 Royal Society of Chemistry. (i) Discharge curves at the current density of 2 mA cm^{-2} in the Al/MnO_2 battery. Reproduced with permission.[28] Copyright 2022 Elsevier.

strong J–T effect of high-spin Mn^{3+}, which distorts the local site symmetry near Mn^{3+} from a regular octahedron and changes the corresponding crystal structure.[65–67] The practical use of layered $LiMnO_2$ in batteries is greatly hindered by severe structural degradation and rapid capacity fading. The small difference in size between Mn^{3+} and Li^+ makes it difficult to form the layered $LiMnO_2$ structure; Mn migration into the Li layer is often observed.[68,69] Thus, an irreversible transition from the layered structure to the spinel structure usually occurs during the first deintercalation. Specifically, the formation of Li vacancies during oxidation results in covalent MnO_2 slab formation and an empty interlayer space with face-to-face O layers. Correspondingly, the Mn ions tend to migrate to the Li layers to homogenize the charge distribution.[70] To realize this transfer process, the Mn ions must cross a tetrahedral interstitial site. Low-spin Co^{4+} (d5), low-spin Co^{3+} (d6), low-spin Ni^{4+} (d6), and low-spin Ni^{3+} (d6) have very strong stability in octahedral sites. However, high-spin Mn^{3+} ions are prone to disproportionate into Mn^{2+} and Mn^{4+}.[71,72] Mn^{2+} (d5) is much less stable in octahedral sites than in tetrahedral sites, promoting movement and thus fast capacity fade. As such, the crystal field stability determines whether the TM ions transfer.[73] Generally, stable redox reactions of monoclinic layered $LiMnO_2$ can be observed at ~3.9 V in the cathodic scan and 3.8 V in the anodic scan (Fig. 4b).[44,74,75] However, the sizes of Na^+ and Mn ions differ, allowing $NaMnO_2$ to form the O3-type layered structure. Meanwhile, there is a great increase in the covalency of the Mn–O bond due to the Na–O bond, which has a much stronger ionic character than the Li–O bond, improving the stability of the tetravalent ions.[70,76,77] First-principles calculations suggest that monoclinic $NaMnO_2$ is stable, whereas $LiMnO_2$ prefers an orthorhombic structure.[78,79] Nevertheless, with the decrease in Na content in Na_xMnO_2, the phase changes from O3-type ($x = 0.9$–1.0) to P2-type ($x = 0.6$–0.8) and P3-type ($x = 0.5$–0.6) oxygen packing.[80] As the P3 and O3 structures share the same MnO_6 octahedral orientation, the layer of O3-type $NaMnO_2$ glides during the deintercalation of Na^+ to form P3-type Na_xMnO_2. This process may be reversible; however, the stress/strain induced by phase transition significantly limits long-term cycling. In addition, Na_xMnO_2 materials exhibit different electrochemical behaviors; many voltage plateaus are observed during the deintercalation/intercalation process due to the ordering of Na^+/vacancy (Fig. 4c).[55,81]

Li-rich MLO materials like O3-type Li_2MnO_3 have attracted extensive attention due to their large capacities, which significantly exceed those of conventional Li-containing cathode materials.[82,83] As such, substantial efforts have focused on utilizing the Li^+ in Li_2MnO_3 with 100% efficiency. The structure of Li_2MnO_3 is usually expressed as $Li[Li_{1/3}Mn_{2/3}]O_2$, consisting of Li layers between MO_2 ($M = Li_{1/3}Mn_{2/3}$) layers, in which one third of the Mn is replaced by Li in a specific honeycomb-like occupation pattern.[84,85] This feature results in excess Li. It is worth noting that Li-rich Mn-based oxide (LRMO) cathode materials are usually synthesized by combining $x$$Li_2MnO_3$ and $(1-x)$$LiTMO_2$ (TM = Ni, Co, Mn), when $x = 0.5$, in the form of $Li_{1.2}Mn_{0.54}Co_{0.13}Ni_{0.13}O_2$.[86,87] However, in addition to the J–T distortion in $LiTMO_2$, the anionic redox reactions triggered by Li_2MnO_3 activation accelerate the migration of Mn ions. These behaviors imply unusual structural degradation,[91–93] including large voltage hysteresis, a gradual decrease in the average voltage during cycling (voltage fade), and an "activation" plateau (4.5 V *vs.* Li/Li^+) during the first charge.[85,94] In the first step of the delithiation process, TM cations are oxidized. At a high voltage between 4.5 and 4.7 V, there is a voltage plateau, and most Li^+ is deintercalated from the material. Meanwhile, in the bulk region, some oxygen anions are oxidized to $O^{(2-x)-}$. The anionic redox is due to the existence of the Li–O–Li configuration, in which unhybridized O 2p states (Li–O–Li states) are generated.[56,95,96] Because the energy of electrons in the Li–O–Li configuration is higher than in the other O 2p states (Fig. 4d), the oxygen in the Li–O–Li configuration is preferentially oxidized at a relatively low voltage of ~4.3 V. It was recently proposed that the Mn can be oxidized from +4 to +7 through three-phase reactions, forming the Mn^{7+} compounds Mn_2O_7 and $LiMnO_4$ and the Mn^{4+} compounds $Li_4Mn_5O_{12}$ and MnO_2.[57] The phase diagrams in Fig. 4e facilitate the understanding of the electrochemical reaction mechanisms of Li-rich MLO materials. However, the detected voltage curves do not follow these three-phase reactions (Fig. 4f), which is mainly attributed to the slow kinetics of these reactions resulting from the long-range diffusion of Mn or O. Compared with Li, the relatively slow migration of Mn leads to the formation of a metastable $Li_{2-x}MnO_3$ compound. The oxygen-redox hypothesis also demonstrates the formation of this metastable phase where the oxygen anion valence states are -1.[56,97]

2.2 Divalent and trivalent ion insertion in MLO materials

Compared with monovalent cations, inserting divalent and trivalent cations in MLO materials can lead to higher energy density. The layered hydrated TM oxide birnessite has attracted tremendous attention because it contains crystal water, which can not only change the interlayered spacing but also weaken the polarizing nature and accelerate the diffusion of divalent and trivalent cations. As the interlayers of birnessite contain multivalent ions and crystal water, their spacing can be expanded to nearly 1 nm, allowing different layered structures to be obtained. Herein, the insertion of divalent and trivalent cations in MLO materials is demonstrated in the context of typical Zn-ion and Al-ion battery applications, respectively.

Zn-ion batteries possess high gravimetric and volumetric capacity (820 mA h g^{-1} and 5854 mA h cm^{-3}). In addition, the excellent reversibility of Zn plating/stripping reactions, safety, and low toxicity make Zn-ion batteries a promising energy storage device. The insertion of Zn^{2+} into birnessite forms the layered δ-Zn_xMnO_2. Alfaruqi *et al.*[27] demonstrated the high capacity of birnessite-based Zn-ion batteries (>250 mA h g^{-1}). Despite the high capacity of layered δ-Zn_xMnO_2 compared with tunnel MnO_2, δ-Zn_xMnO_2 still has low capacity retention during electrochemical processes. Recent research demonstrated that the capacity decay is due to the phase transition from the layered structure to the spinel structure and the dissolution of Mn ions in electrolytes.[98] Wang *et al.*[58] prepared a mesoporous layered MnO_2 nanosphere with H_2O and Zn^{2+} in the interlayers

(Fig. 4g and h), which had a high specific capacity (358 mA h g^{-1} at 0.3 A g^{-1}). In addition, *in situ* and *ex situ* characterizations have been used to uncover the structural changes of Zn_xMnO_2 during charge/discharge cycling. Energy storage mechanism that involves the co-insertion/extraction of H^+ and Zn^{2+} along with the deposition/dissolution of zinc sulfate hydroxide hydrate on the electrode surface was discovered. In general, the specific structural degradation between Zn-batteries in aqueous solution and Li/Na-batteries in the organic solution is different due to their different electrolytes and inserted ions. Compared with the inserted Li^+ or Na^+ with monovalence, divalent Zn^{2+} has much higher electrostatic repulsion and atomic radius, which inevitably causes larger volume change of MLO materials during the electrochemical processes and thus results in more severe layered structure distortion than the insertion of Li^+/Na^+ into MLO materials.[99,100] The electrolytes used in Zn batteries are always acidic, in which higher H^+ concentration exists. As a result, MLO materials suffer from the more serious dissolution issues of Mn^{2+} originating from the disproportionation reaction than the organic electrolyte that has low H^+ concentration used in Li/Na-batteries. In addition, Alfaruqi *et al.* proposed that layered MnO_2 in the process of Zn-ion insertion undergoes a series of structural transformations: layered MnO_2–layered Zn_xMnO_2–Zn-inserted phase–spinel $ZnMn_2O_4$.[98] Although the phase transition during the discharging can be reverted to the layered MnO_2 during the initial charging, these phase transformations may induce the huge change of layered structure and thus easily results in the structural degradation during the long-term cycles, which is demonstrated by the complete phase transformation from the layered structure into the spinel structure after prolonged cycles. Additionally, the co-intercalation mechanism of H^+ and Zn^{2+} has been demonstrated.[101] Unfortunately, the effect of co-intercalation of H^+ and Zn^{2+} on structural degradation is not clear until now. But it must cause different degradation mechanisms compared with the single Li^+/Na^+ insertion in Li/Na-batteries.

Al-based batteries, which have three-electron redox states (from Al^{3+} to Al) and are low cost and easy to handle, provide an alternative to commercial Li/Na-ion batteries. Birnessite, with large interlayer spacing, enables the reversible intercalation and extraction of Al^{3+}, which can deliver high capacity. However, the discharge rate is relatively low in this layered structure due to the sluggish diffusion kinetics of Al^{3+} in the interlayers. The strong electrostatic interaction between Al^{3+} and oxygen in layered birnessite can result in the formation of inactive Al_x-MnO_2 and, subsequently, fast capacity decay. Therefore, it is crucial to prevent the direct insertion of Al^{3+} ions into the lattice. To address these issues, electrolyte engineering has been proposed to tune the solvation structure of Al^{3+}. For example, Xu *et al.*[28] developed an Al-based battery with high stability by tuning the electrolyte. When 1 M $MnCl_2$ and 4.4 M $AlCl_3$ were used, the intercalation of Al^{3+} was prohibited because of the large solvation structure of $AlCl_{1.8}(H_2O)_{4.2}{}^{1.2+}$ that formed in this electrolyte.[28] Correspondingly, the Al–MnO_2 batteries delivered a large specific capacity of 493 mA h g^{-1} and stable cycling behaviors over 1000 cycles, demonstrating the potential of trivalent ion-based energy storage (Fig. 4i).

3. Degradation mechanisms

J–T distortion, which elongates the two axial Mn–O bonds, induces MnO_6 to transform from the cubic form into the tetragonal form. This atomic structure evolution influences the physicochemical properties of MLO materials and impacts their electrochemical performance. Generally, the degradation issues caused by J–T distortion in MLO cathodes can be divided into (i) irreversible phase transition, (ii) dissolution/disproportionation reaction, (iii) interfacial degradation arising from Mn^{2+}, and (iv) crack formation. As a result, a comprehensive understanding of these problems is necessary for developing MLO-based energy storage devices with high structural stability and prolonged life spans.

3.1 Irreversible phase transformation

3.1.1 Layered-to-tunnel/spinel phase transition. Birnessite with layered packing composed of edge-sharing [MnO_6] octahedra can convert to other types of tunnel structures during the electrochemical process. At the beginning of phase transition, crystal water migrates out of the interlayer spaces. The layered structure collapses during the oxidation of Mn^{2+} to Mn^{3+} to Mn^{4+} or the disproportionation of Mn^{3+} ions to Mn^{2+} and Mn^{4+} ions. As a result, the [MnO_6] octahedral layers are distorted and rearranged, which reduces lattice stress and causes the layer-to-tunnel phase transition (Fig. 5a).[88,102] Subsequently, the destroyed layers may interlink again to form a new phase of α-MnO_2, or other tunnel phases may be formed in an analogical process. The irreversible phase transition from the layered structure to the spinel structure is considered the main reason for the severe electrochemical degradation of MLO cathodes. Specifically, the layered structures of MLO materials prefer to transform into spinel-like structures when alkali ions are removed from the interlayers. This phase transition originates from the rearrangement of Mn and alkali ions and is thus generally irreversible, causing rapid electrochemical performance decay.[98,105–107] In addition, the high mobility of Mn^{2+} in $LiMnO_2$ accelerates the transformation from the layered structure into the spinel structure during the first charge.[108,109] Mn ions can move into tetrahedral sites as vacancies are generated in the Li layer.[106] Meanwhile, the Li/Mn dumbbell configuration is generated (Fig. 5b) when the Li ions migrate to a tetrahedral site in an adjacent Li layer,[48] which endows the Mn in tetrahedral sites with high stability and serves as a nucleus for the layered-to-spinel phase transition.

Gu *et al.*[89] reported that newly formed spinel domains show random orientation within the same particle during cycling. The extraction of Li^+ ions together with the loss of oxygen from Li_2MnO_3 induces the displacement of TM cations. This change further destroys the lattice and creates numerous nanometer-scale spinel particles, leading to rapid capacity and voltage decay. Correspondingly, Li^+ ions cannot intercalate in the transformed structure again, resulting in low initial coulombic efficiency. For example, in the first oxidation process, atomic columns in the Li layers can be observed in both the surface and bulk regions. This feature implies the migration of TM ions to

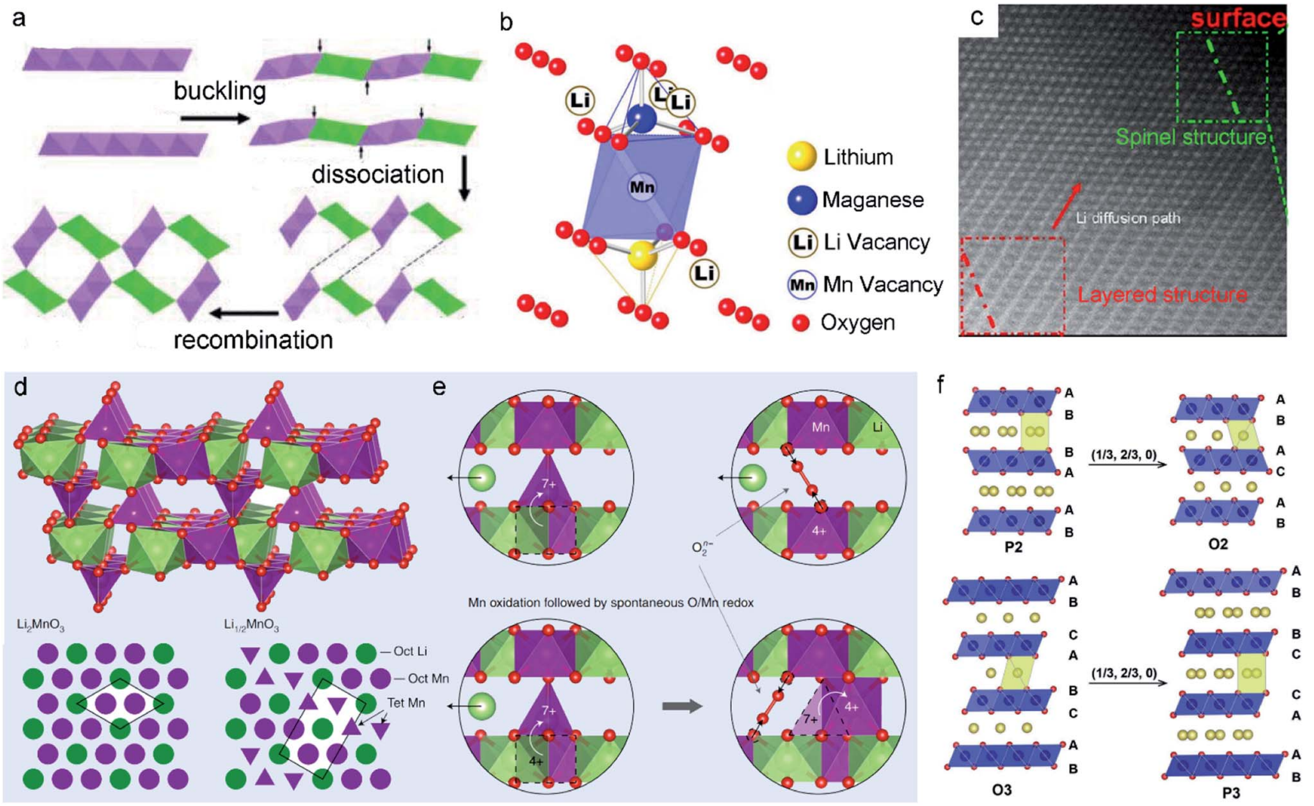

Fig. 5 (a) Schematic illustration of the phase transformation process of the layer into tunnel through layer buckling. Reproduced with permission.[88] Copyright 2011 American Chemical Society. (b) Schematic illustration of the Li/Mn dumbbell configuration. Reproduced with permission.[48] Copyright 2011. The Electrochemical Society. (c) Phase transition from the layered structure to the spinel of cycled layered LNMO after 100 cycles. Reproduced with permission.[89] Copyright 2013 American Chemical Society. (d) Proposed $Li_{1/2}MnO_3$ structure showing the Li_2MnO_3 cathode material component at the end of the activation plateau. (e) The charge mechanisms in Li-rich MLO oxides. Reproduced with permission.[57] Copyright 2019 Springer Nature. (f) Schematic illustration of the layered Na-containing oxides for P2-type, O2-type, O3-type, and P3-type stackings. Reproduced with permission.[90] Copyright 2017 Wiley-VCH.

the Li layer (Fig. 5c). Meanwhile, the development of pores and cracks among the layered nanoparticles results in lattice degradation and vacancy formation upon the extraction of Li^+ ions, suggesting that the layered-to-spinel phase transition is a nucleation and growth mechanism. Recently, Radin *et al.*[57] modeled the irreversible phase transition. As shown in Fig. 5d, a typical local configuration forms upon Li_2MnO_3 charging. Mn^{4+} remains in the $[MnO_6]$ octahedral sites, while Mn^{7+} tends to migrate to the tetrahedral sites in $Li_{1/2}MnO_3$. To form $Li_{1/2}MnO_3$, half of the Mn ions must migrate, with one quarter moving downward and one quarter moving upward (Fig. 5e). This behavior finally produces an unstable lattice structure.

3.1.2 P/O phase transition. Unlike Li_xMnO_2, Na_xMnO_2 does not easily transform from the layered phase into spinel structures.[48] This difference in structural evolution is attributed to the fact that Na^+ does not favorably occupy the tetrahedral site in $NaMnO_2$ because it is larger than Li^+. Therefore, with Na^+, the transformation from layered to spinel structures is unfavorable, and the layered Na_xMnO_2 is highly metastable. Nevertheless, a series of phase transformations can occur in the P2-type and O3-type Na_xMnO_2, changing the stacking sequences during the electrochemical processes. If some Na^+ ions are removed, P2-type Na_xMnO_2 transforms to O2-type Na_xMnO_2, deriving from the gliding ($\pi/3$ rotation) of some MnO_6 octahedra sheets. This behavior contracts the crystal structure and decreases the interlayer distance (Fig. 5f).[90]

As the large Na^+ ions stabilize the prismatic sites in the P2 phase, MnO_2 slabs tend to form octahedral sites, enabling the phase change from P2 to O2.[90] For the O3-type phase, when a sufficient amount of Na^+ is removed from the interlayers, MnO_2 sheet gliding induces the formation of broad prismatic sites. The stacking of oxygen transits to AB, BC, CA, known as the P3 phase. In other words, the extraction of Na^+ from both P2 and O3 phases generally causes the gliding of MnO_2 sheets, promoting the phase transition (layer-to-layer). Na_xMnO_2 has a more complicated phase than its Li analogs due to the large size of Na^+ coupled with the ordering arrangement of Na^+ and vacancies. Because the MnO_2 sheet gliding combined with the change in oxygen stacking brings severe structural degradation, cracks are often observed in Na_xMnO_2 during cycling. Therefore, reducing or suppressing these phase transformations is critical for improving the electrochemical performance.

3.2 Dissolution/disproportionation reaction

The J–T effect modulates the Mn–O bond lengths, and the strength of this distortion is related to the covalency of the Mn–

O bonds. In contrast to the shorter axial Mn–O bonds, longer axial Mn–O bonds with weaker overlap have a higher negative charge (Fig. 6a).[103] From a Lewis acid–base perspective, the axial oxygen atoms enhance the Lewis base strength and thus have high reactivity with acid. Generally, the electrolytes contain substantial H$^+$, and these ions exclusively attack the axial oxygens that possess higher negative charges, resulting in severe Mn dissolution. For example, in Li-ion batteries, the $LiPF_6$ salt in the electrolyte is prone to hydrolysis, and this process induces the formation of a strong Lewis acid, HF. The H$^+$ in HF interacts with the elongated axial oxygens, generating H_2O through oxide protonation. Meanwhile, an electron must transfer from the Mn to the axial oxide orbital; this charge transfer derives from the $(d_{z^2})^1$ orbital of Mn^{3+}. Correspondingly, the protonation process along with a metal-to-ligand electron transfer increases the oxidation state of the Mn ions. Unfortunately, the formed Mn^{4+} ions are a strong oxidizer that can be directly converted to the J–T-stabilized free state (Mn^{2+})

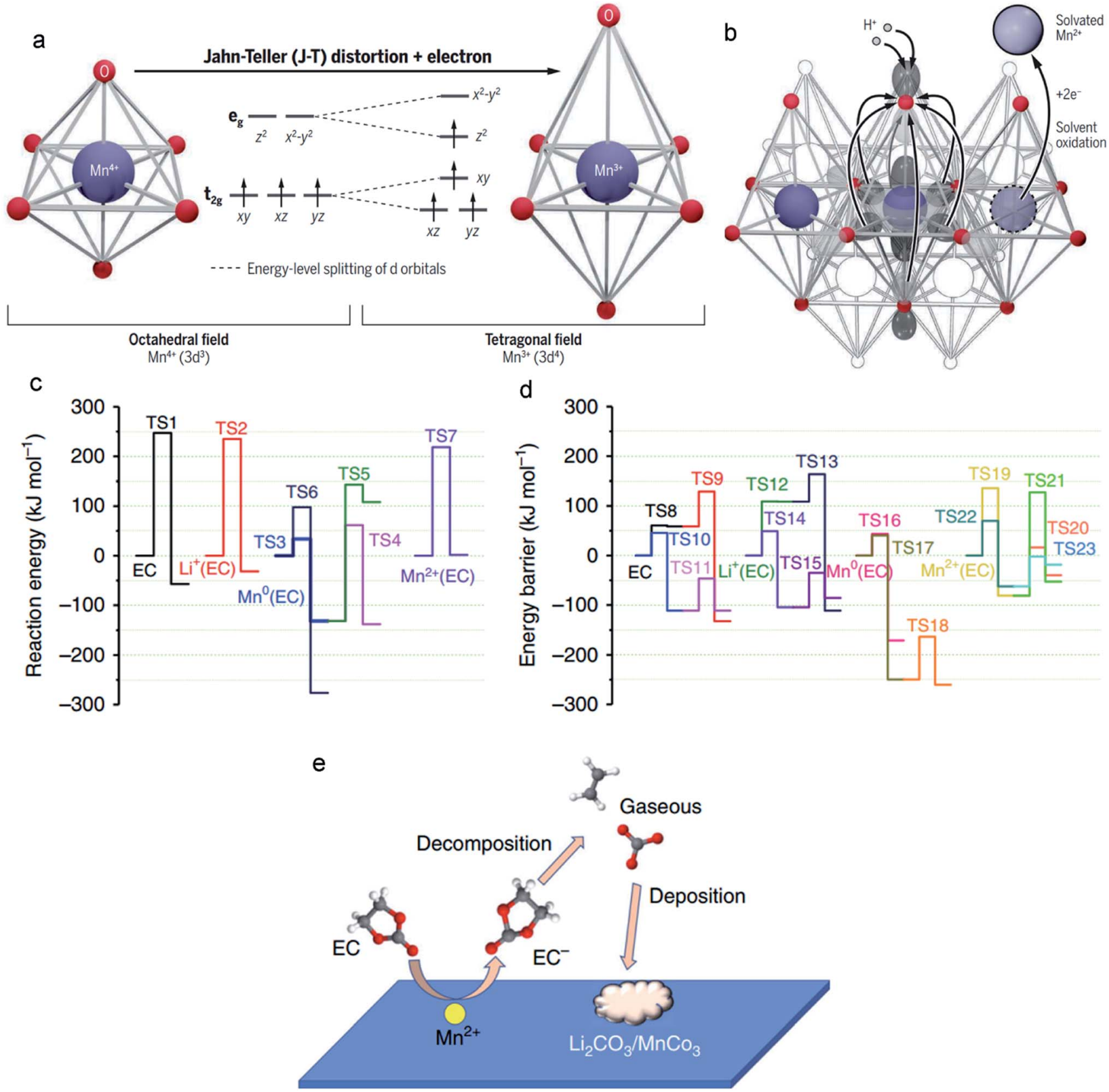

Fig. 6 (a) The six equivalent Mn–O bonds (left) in MLOs are distorted and transformed into the four shorter equatorial bonds and two longer axial bonds (right). (b) H$^+$ in the electrolyte attacks the axial oxide and transfers electrons from the manganese to oxygen. Reproduced with permission.[103] Copyright 2020 American Association for the Advancement of Science. (c and d) Decomposition reaction of EC in electrolytes with/without interacting with metallic Mn, Mn^{2+}, and Li$^+$ before and after one-electron reduction. (e) The catalytic effect of Mn^{2+} on the decomposition of electrolytes. Reproduced with permission.[104] Copyright 2019 Springer Nature.

via a disproportionation reaction (the two-electron reduction pathway), and Mn^{2+} ions are easily dissolved into the electrolyte (Fig. 6b).

3.3 Interfacial degradation arising from Mn^{2+}

Electrochemical degradation mechanisms originate from not only altering the surface structure of the MLO materials by the dissolution/disproportionation reaction, but also deteriorating the anode interface by the impact of Mn^{2+}. The electric field force and/or concentration gradient drives the Mn ions in the electrolyte to the anode side where Mn ions tend to change the interface compositions by decomposing the electrolytes and/or depositing on the anode,[111] resulting in interfacial degradation and electrochemical degradation.

Specifically, the lower operation potential of conventional anodes like Li metal and graphite compared with the redox potential of Mn/Mn^{2+} results in the electroplating of soluble Mn^{2+} in the electrolyte on the anode. Simulations have indicated that the deposited Mn on the anode has high electrical conductivity or electrocatalytic properties, accelerating the decomposition of the electrolyte.[112–114] The reconstructed SEI gradually covers the anode and affects the ionic diffusion kinetics. Recently, Wang *et al.*[104] demonstrated that overlooking the effect of the solvation sheath on the Mn^{2+} ions is the main reason for the inaccurate conclusions that Mn is the final product of the anode. They proposed that the solvation sheaths around Mn^{2+} act as molecular-sized reaction vessels, in which the central Mn^{2+} activates its solvation member and guides the reaction process. This process explains why Mn atoms are rarely detected on anodes.[115,116] If the solvation sheath begins to lose solvating members, Mn^{2+} ions can convert to Mn atoms, explaining the existence of Mn atoms on the surface of the anode. It was found that the Mn atoms (Fig. 6c) substantially decrease the activation energy of EC decomposition (from TS1 247.20 to TS3 33.69 kJ mol^{-1}). In particular, when coordinated with Mn^{2+}, the EC decomposition activation energy (TS7) is less than that of neat EC (TS1), which is only 16.57 kJ mol^{-1}. After the EC anion receives an electron, the decomposition of EC (TS10) becomes much easier (Fig. 6d). With Mn^{2+}, the reduced EC decomposition activation energy (TS21: 9 kJ mol^{-1}) is higher than that of reduced EC (TS10), suggesting that the EC anion moves away from Mn^{2+} after receiving one electron. Nevertheless, the generated coordination vacancies around Mn^{2+} become occupied by other incoming EC molecules. Overall, the Mn^{2+} solvation sheath serves as a catalytic center on the electrode surface or in the electrolytes, which continuously accelerates the reduction of carbonate molecules, resulting in severe interfacial degradation, and cell performance fading (Fig. 6e).

3.4 Crack formation

It has been proven that the ion intercalation/deintercalation process causes the expansion and contraction of the structure, generally resulting in a high strain on the materials that gradually induces cracking and disintegration.[117,118] Moreover, irreversible phase transition and Mn dissolution have been demonstrated to cause crack formation and severe capacity degradation.[119] Therefore, the observed macroscale cracks originate from the evolution of the atomic-scale structure.[120] By deeply analysing the atomic structure change, we can elucidate the crack formation process. Recently, Sharififi-Asl *et al.*[110] used aberration-corrected scanning transmission electron microscopy to demonstrate the correlation between the atomic structure evolution during the electrochemical cycling of LRMO materials and the formation of cracks. They observed a spinel-type grain boundary derived from the migration of TM ions to the Li-octahedral sites (Fig. 7a). Strain analysis revealed that the spinel-type grain boundary had a high strain, which may serve as crack initiation points in the cycled LRMO (Fig. 7b). Furthermore, a nanocrack was observed initiating on the grain boundary, which could develop into a large-scale crack in the cathode during further cycling. Apart from the irreversible phase transition from the layered structure to the spinel or rock-salt phase, a disordered phase was also observed (Fig. 7c). The energy-dispersive spectroscopy map shows Ni enrichment and Mn depletion in the disordered area (Fig. 7d). The depletion of Mn is attributed to the dissolution of Mn at the high-energy grain boundaries, which further accelerates the diffusion of Ni toward these Mn vacancies.

4. Remedies for electrochemical degradation in MLO cathodes

Numerous endeavors have been devoted to developing strategies at the atomic level to improve MLO-based energy storage performance. These strategies can be classified into the following categories: (i) elemental doping; (ii) interlayered structure manipulation; (iii) vacancy introduction; (iv) novel structural design. In this section, various strategies, synthesis methods, improved mechanisms, and electrochemical properties of typical MLO materials have been discussed and summarized, as shown in Table 2.

4.1 Elemental doping

Incorporating different foreign ions into MLO materials is a common practice for optimizing their intrinsic properties. Elemental doping, including anion and cation doping, has been demonstrated to significantly boost the structural stability of MLO materials, which not only changes the electronic structure but also suppresses irreversible phase transformations during ion intercalation/deintercalation. Various dopants have been proposed, including cationic dopants (Cr, Ta, and Al) and anionic dopants (F and Br).[24,34,121–123]

Inferior structural stability and electronic conductivity have been demonstrated to limit the electrochemical performance of δ-MnO_2. Zhao *et al.*[124] proposed that incorporating Cr^{3+} into δ-MnO_2 could boost its rate capability and cycling stability within the potential window of 0–1.2 V (*vs.* Ag/AgCl). δ-MnO_2 without Cr doping undergoes severe J–T distortion, which increases the average Mn–O bond length and accelerates the migration and dissolution of Mn. Numerous dissolved Mn ions in the electrolyte generate cracks and pulverize the MnO_2 nanosheet fragments to a moderate extent (Fig. 8a). In addition, the

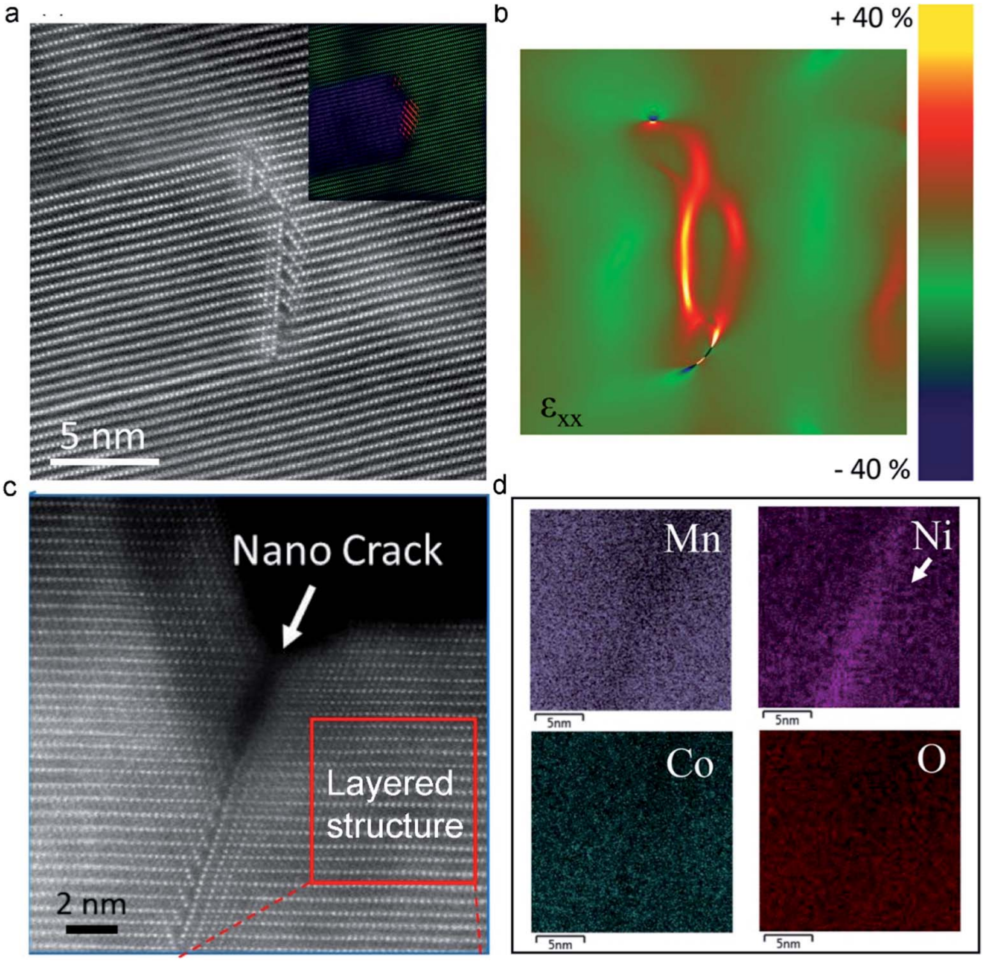

Fig. 7 (a) The HAADF image of the pristine cathode material, forming a spinel-type grain boundary. (b) The generation of a large strain in the spinel-type grain boundary analyzed by Geometrical Phase Analysis (GPA). (c) Atomic resolution image of a nanocrack at the particle surface induced by a spinel-type grain boundary. (d) EDS maps collected from the nanocrack. Reproduced with permission.[110] Copyright 2019 American Chemical Society.

dissolved Mn ions form a precipitate in the electrolyte, impacting the electrochemical performance of the whole cell. Meanwhile, buckled Mn–O slabs are formed along with the J–T distortion, and these slabs dissociate and rearrange, leading to the irreversible phase transition from a layered structure to a 2 × 2 tunnel structure.[88] Correspondingly, only 69.1% of the capacity of the pristine δ-MnO_2 electrode is retained over 10 000 cycles at the current density of 10 A g^{-1}. The elongation of the Mn–O bond induced by the J–T distortion is effectively suppressed in Cr^{3+}-doped δ-MnO_2 (Fig. 8b), implying that the Mn ion migration barrier greatly increases. The reinforced birnessite shows significantly improved structural stability (82.6% capacity retention over 30 000 cycles) in comparison with the pristine δ-MnO_2, demonstrating the excellent effect of Cr doping in δ-MnO_2 on suppressing the J-T effect and stabilizing the layered structure. Moreover, owing to the improved effect of Cr on the electronic conductivity of δ-MnO_2, the Cr-doped δ-MnO_2 showed a much higher capacity of 250 F g^{-1} than pristine δ-MnO_2 with 178 F g^{-1} at the current density of 0.2 A g^{-1} with a high mass loading of ~5 mg cm^{-2}.

To further validate the role of elemental doping, Zhang *et al.*[34] modeled the Zn-doped layered $Na[Li_{0.25}Mn_{0.75}]O_2$ material to explore its effect on thermodynamics and the electronic structure. Zn doping enables the oxidation of the Mn^{3+} center and thus increases the Mn^{4+} content of the centers in the Zn-doped materials (Fig. 8d). As a result, the materials are more structurally stable and undergo less J–T distortion, leading to negligible capacity decay of the Zn-doped layered $Na[Li_{0.25}Mn_{0.75}]O_2$ electrode (99% capacity retention over 200 cycles), which is much higher than that of the pristine $Na[Li_{0.25}Mn_{0.75}]O_2$ electrode (41% capacity retention over 200 cycles). From the perspective of thermodynamics, the formation energies of mixing enthalpy (ΔH_{mix}) have an important influence on phase stability. The calculated thermodynamic energy values can confirm the structural stability of materials according to charge carrier content. Fig. 8e shows that $Na[Li_{0.25}Mn_{0.75}]O_2$ comprises five ground states, whereas Zn-doped $Na[Li_{0.25}Mn_{0.75}]O_2$ has seven ground states. Specifically, in the first region (x = 0–0.25), Zn doping can decrease ΔH_{mix}, indicating a reduced volumetric strain (Zn-doped structure: $\varepsilon_V = -0.027$;

Table 2 The synthesis methods and electrochemical performance of different strategies

Material	Strategy	Synthesis method	Improved mechanism	Capacity	Capacity retention	Ref.
δ-MnO_2	Cr doping	Hydrothermal	Suppressing the elongation of the Mn–O bond	250 F g^{-1} at 0.2 A g^{-1}	69.1% (10 000 cycles) *vs.*82.6% (30 000 cycles) at 10 A g^{-1}	124
$Na_{0.65}Mn_{0.75}Ni_{0.25}O_2$	F doping	Solid-state reaction	Inhibiting P3–O1 phase transition	160 mA h g^{-1} at 0.1C	75.1% *vs.* 83.1% (100 cycles) at 0.2C	125
$Na_{0.833}[Li_{0.25}Mn_{0.75}]O_2$	Zn doping	Sol–gel method	Inhibiting P2–P2′ phase transition	241 mA h g^{-1} at 0.2C	41.3% *vs.* 96.9% (200 cycles) at 0.2C	34
$Na_{0.65}Mn_{0.75}Ni_{0.25}O_2$	F/B co-doping	Solid-state reaction	Suppressing P3–O1 phase transition	164 mA h g^{-1} at 0.1C	86% *vs.* 75% (100 cycles) at 0.2C	125
$Na_{0.5}MnO_2$	Na^+ preintercalation	Hydrothermal	Stabilizing the interlayered structure	366 F g^{-1} at 1A g^{-1}	96% (10 000 cycles) at 4 A g^{-1}	126
δ-MnO_2	Polyaniline intercalation	Chemical oxidation and reduction	Strengthening the layered structure and eliminating layered−spinel phase transition	280 mA h g^{-1} at 0.2 A g^{-1}	89.2% (5000 cycles) at 2 A g^{-1}	101
$Na_{0.67}Mn_{0.5}Co_{0.5-x}Fe_xO_{2.}$	Fe^{3+} preintercalation	Solid-state reaction	Restraining the potential slab sliding	160 mA h g^{-1} at 0.2C	68.2% *vs.* 89.6% (100 cycles) at 10C	127
$Na_{2/3}[Zn_{1/9}Mn_{7/9}\square_{1/9}]O_2$	Mn vacancy	Pechini method	Shortening the Mn–O bond length	204 mA h g^{-1} at 0.02 A g^{-1}	43.4% *vs.* 25.6% (100 cycles) at 0.02 A g^{-1}	128
$Li_{1.22x}Na_xMn_{0.56}Ni_{0.16}Co_{0.08}O_2$	O vacancy	Solid-state reaction	Modulating the local Mn coordination environments	250 mA h g^{-1} at 0.1C	84% *vs.* 94% (100 cycles) at 0.5C	40
$Li_{1.2}[Mn_{0.66}Co_{0.17}Ni_{0.17}]_{0.8}O_2$	Mixed vacancies of O and TM	Solid-state reaction	Prohibiting the O3–P3 phase transition	220 mA h g^{-1} at 0.02 A g^{-1}	86% (250 cycles) at 0.125 A g^{-1}	129
$NaMnO_{2-y\ -\delta}(OH)_{2y}$	Novel monoclinic phase	Hydrothermal sodiation	Decreasing the volume change *via* a stable interlayer	215 mA h g^{-1} at 0.2C	94.6% (1000 cycles) at 10C	47
Spinel–layered $LiMnO_2$	Heterostructure construction	Electrochemical conversion	Modulating interfacial orbital ordering	286 mA h g^{-1} at 1C	90.4% (2000 cycles) at 12C	44
$Li_2Mn_{2/3}Nb_{1/3}O_2F$	Disordered structure	Ball-milling	Replacing the anionic reaction with a Mn reaction	320 mA h g^{-1} at 0.01 A g^{-1}	90% (25 cycles) at 0.02 A g^{-1}	130
$Li_{1.2}Ni_{0.2}Mn_{0.6}O_2$	Surface structure design	Chemical vapor deposition	Charge compensation	238 mA h g^{-1} at 0.5C	99% (100 cycles) at 1C	131

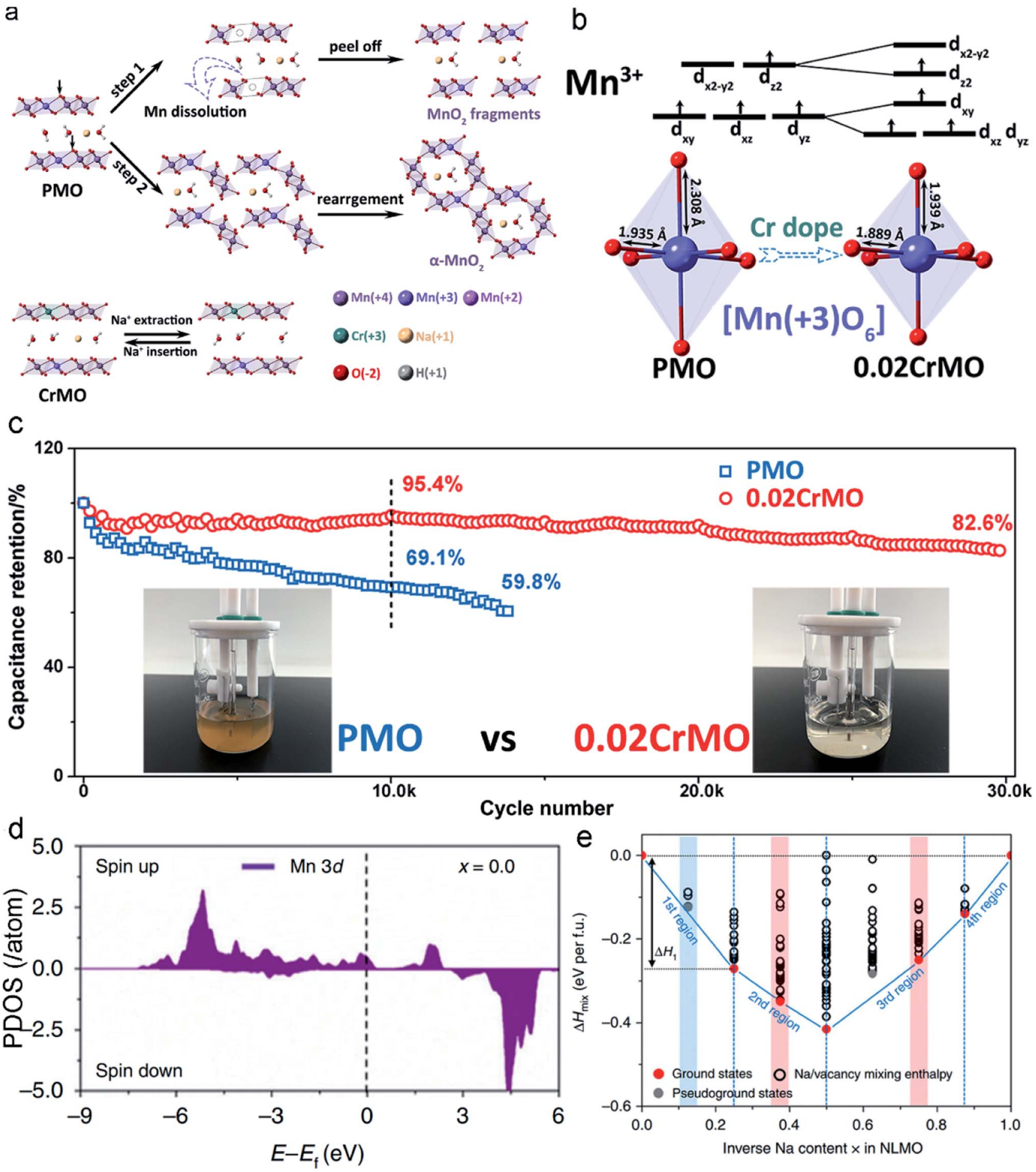

Fig. 8 (a) Mechanisms of Cr-doping for the stabilities of the δ-MnO_2. (b) The shortened Mn–O bonds after Cr-doping. (c) Cycling performances of the pristine δ-MnO_2 and Cr-doping δ-MnO_2 electrodes at a current density of 10 A g^{-1}. Reproduced with permission.[124] Copyright 2020 Royal Society of Chemistry. (d) The PDOS of the Mn^{3+} sites in the layered Zn-doping $Na[Li_{0.25}Mn_{0.75}]O_2$. (e) The two atomic models include 8 Na atoms in each unit cell. Reproduced with permission.[34] Copyright 2019 Springer Nature.

undoped structure: $\varepsilon_V = -0.04$). In the second region ($x = 0.25$–0.50), Zn-doped $Na[Li_{0.25}Mn_{0.75}]O_2$ is illustrated by the red circles located on the tie line, which directly confirm that desodiation occurs in the same phase. In undoped $Na[Li_{0.25}Mn_{0.75}]O_2$, a pseudo-ground state appears, suggesting the formation of a new phase during the desodiation process. In the third region ($x = 0.50$–0.88), Zn-doped $Na[Li_{0.25}Mn_{0.75}]O_2$ has one pseudo-ground state as marked by the grey circle ($x = 0.63$), indicating that phase dissociation may occur within the narrow region from $x = 0.5$ to $x = 0.75$. The extra ground states in Zn-doped $Na[Li_{0.25}Mn_{0.75}]O_2$ are beneficial for suppressing the inherent phase transition that occurs in $Na[Li_{0.25}Mn_{0.75}]O_2$.[132] In contrast to its doped counterpart, two pseudo-ground states of undoped $Na[Li_{0.25}Mn_{0.75}]O_2$ are shown as grey circles above the tie line (at $x = 0.63$ and $x = 0.75$, respectively), reflecting the phase separation to this extent during desodiation.

In summary, elemental doping can restrain the elongated bonds and stabilize the metastable structure to inhibit J–T distortion by changing the atomic structures around Mn ions, giving rise to a more stable structure. Additionally, the average valence of Mn ions may be tuned to above +3.5, which is beneficial to suppress the J–T effect, such as the introduction of the low-valence ions. Although elemental doping has achieved tremendous progress, some concerns should be noted. Presently, annealing at high temperatures is the most popular method to realize doping, but this process involves high energy cost and has low efficiency. In addition, it is difficult to precisely control the doping content and doping sites. Hence, it is highly desirable to explore the powerful and facile method of accurate doping with low energy costs.

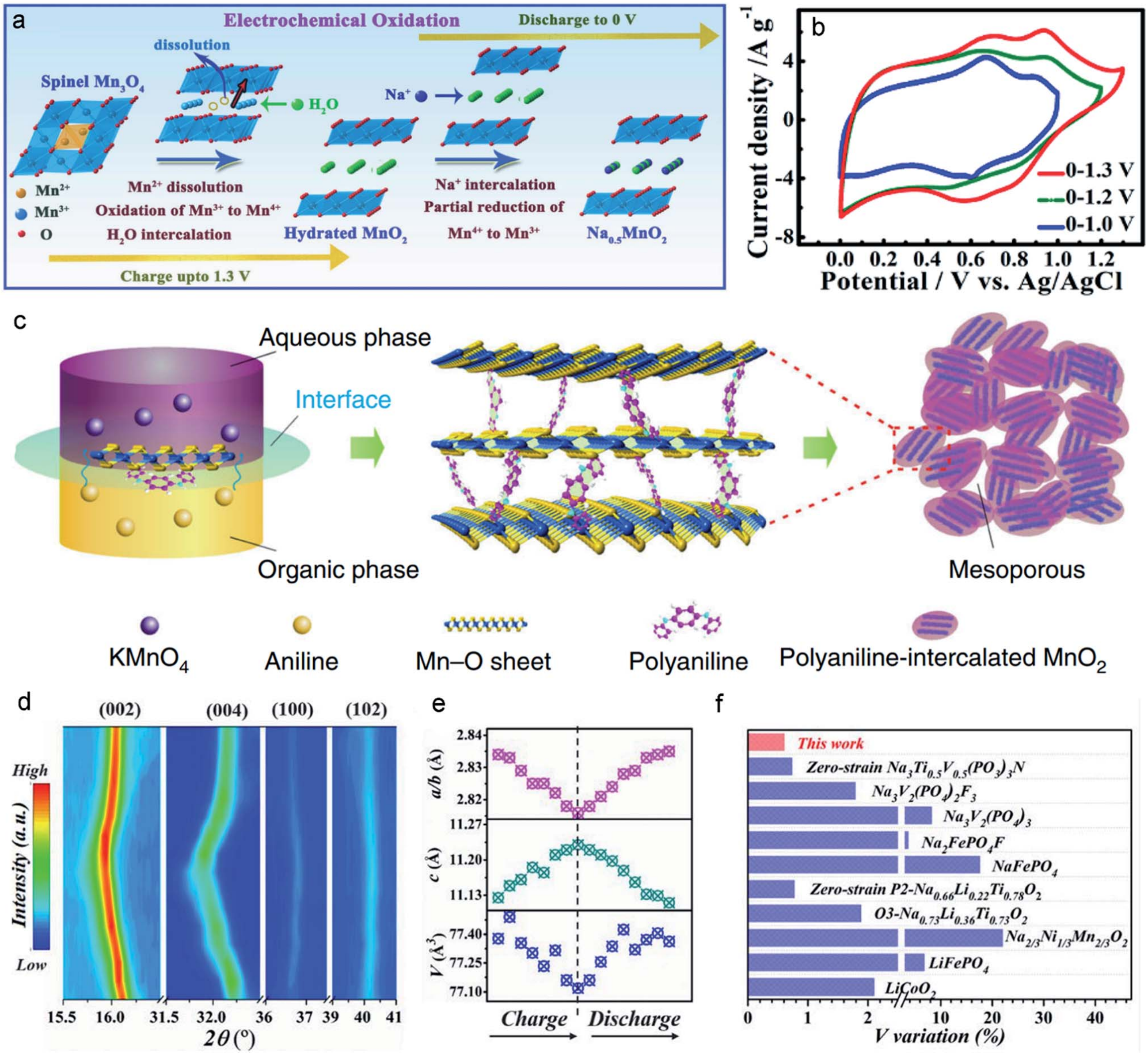

Fig. 9 (a) Schematic illustration of the preintercalation process during the electrochemical oxidation. (b) The ion-preintercalation effect on widening the potential windows of layered $Na_{0.5}MnO_2$. Reproduced with permission.[126] Copyright 2017 Wiley-VCH. (c) A schematic of the expanded structure by the intercalation of polyaniline (PANI) into MnO_2 nanolayers. Reproduced with permission.[101] Copyright 2018 Springer Nature. (d) The typical *in situ* XRD patterns of the $Na_{0.67}Mn_{0.5}Co_{0.5-x}Fe_xO_2$ electrode. (e) The variation of cell parameters *c* (green points), *V* (blue points), and *a*/*b* (pink points). (f) *V* variation of $Na_{0.67}Mn_{0.5}Co_{0.5-x}Fe_xO_2$ and several typical sodium-storage cathode materials during the charge/discharge process. Reproduced with permission.[127] Copyright 2021 Wiley-VCH.

4.2 Interlayered structure manipulation

Most MLO materials undergo the degradation of diffusion channels after long-term cycling processes. Therefore, the stabilization/enlargement of diffusion channels has emerged as a promising strategy based on improving the stabilization of the interlayer to accommodate J–T distortion. One of the characteristics of preintercalation in the interlayer hosts of MLO materials is the expansion of the interlayer spacing. The appropriate intercalated ions in the interlayer can serve as pillars to effectively expand and support this diffusion channel.[24,133] Xia and co-authors[126] proposed a hydrothermal synthesis to preintercalate Na^+ into birnessite and prepared a high Na content birnessite ($Na_{0.5}MnO_2$) (Fig. 9a). It is known that preintercalating the Na^+ protects the layered structure from collapsing. Meanwhile, the enhanced Na content in birnessite also extends the potential window from 0–1.0 V to 0–1.3 *vs.* Ag/AgCl (Fig. 9b). In addition, owing to the high diffusion kinetics of Na^+ in large interlayers, the $Na_{0.5}MnO_2$ electrode could achieve a high rate performance and specific capacitance (366 F g^{-1} at 1 A g^{-1}; 231 F g^{-1} at 16 A g^{-1}). A 2.6 V aqueous energy storage system and large energy density of 81 Wh kg^{-1} serve as further evidence that preintercalating Na^+ ions into the interlayer can boost its energy storage. In addition to the preintercalation of ions into the diffusion channel, preintercalation of molecules can also effectively expand the interlayer space. Huang *et al.*[101] prepared a polyaniline-intercalated layered MnO_2 *via* an aqueous/organic interfacial reaction. In detail, the chemical reduction of $MnO_4{}^{2-}$ and the oxidation polymerization of aniline occur at the same time at the interface between the inorganic phase ($KMnO_4$ aqueous solution) and the organic phase (CCl_4-containing aniline monomer), inducing the layer-by-layer assembly of polyaniline and MnO_2 (Fig. 9c) with a dramatically expanded interlayer (~1.0 nm). The large interlayer spacing of PANI-intercalated MnO_2 achieved the best rate capability (280 mA h g^{-1} at the current density of 0.2 A g^{-1}; 110 mA h g^{-1} at the current density of 23 A g^{-1}) among the reported data in this field.[77,134,135] Additionally, intercalating the PANI into the interlayers significantly reinforces the layer structure, thus avoiding irreversible phase transition and the distortion of the interlayered structure, as evidenced by the outstanding long-term cycling stability over 5000 cycles in rechargeable Zn–MnO_2 batteries.

Aside from enlarging the interlayer spacing, some intercalated ions may have a pinning effect to suppress phase transitions and thus improve the structural stability. In Na-ion batteries, Na^+ ions possess a large radius and cause huge lattice changes of more than 20% during the sodiation/desodiation process, inducing a severe phase transition, resulting in more than 30% capacity fading over 100 cycles at the current density of 2C.[127] Chu *et al.*[127] reported that intercalated Fe in the Na site acts as a pinning point to suppress slab sliding. The pinning point represents a structural stabilizer that significantly reduces the volume variation to appropriately 0.6% (Fig. 9d and e). This slight structural change confers outstanding structural stability and maintains a smooth channel for fast Na-ion transfer during the electrochemical processes. The ultra-low volume variation is even smaller than those of electrode materials like $LiCoO_2$ and $LiFePO_4$, as shown in Fig. 9f. Consequently, Na-ion batteries fabricated using this improved material can achieve high capacity retention of ~89.1% over 100 cycles at the current density of 2C. Impressively, 71% capacity can be retained over 1000 cycles at the high current density of 10C.

On the basis of the above introduction, manipulating the interlayered structure *via* the preintercalation can greatly enlarge the interlayer space and thus facilitate the ions to diffuse in the bulk of the MLO materials, which also enables the MLO materials to provide more active sites to accommodate cations. In addition, the support effect of preintercalated ions/molecules on the interlayered structure can improve the structural stability, guaranteeing long-term cycling stability. Nevertheless, preintercalated ions may have the electrostatic repulsion effect with the inserted ions during the electrochemical processes. Moreover, the stability of supported ions/molecules should be considered. These preintercalated species suffer from issues of extraction of ions/molecules from the host interlayers during the electrochemical processes, which is unavoidable. Such issues eliminate the advantages of manipulating interlayered structures and induce severe structural degradation during the continuous intercalation/de-intercalation of cations. Excessive cation preintercalation would induce the phase transition where the structural reconstruction enables the loss of the fast ionic transport of layered pathways.[100] Therefore, to avoid these disadvantages, careful screening of the preintercalated ions/molecules and optimizing their amount are necessary.

4.3 Vacancy introduction

Considering that vacancy engineering can tune the physicochemical properties of MLO materials, it is logical to anticipate that precisely designing vacancies may promote their electrochemical performance. Vacancies involving MLO materials mainly consist of anionic (nonmetal) vacancies, cationic (metal) vacancies, and mixed vacancies. MLO materials usually suffer from severe J–T distortion of the octahedral Mn^{3+} at low voltages and/or anionic reaction-induced structural evolution at high potentials. Incorporating the vacancies into the TM layer promotes ionic reduction/oxidation and bond length changes, which have a significant effect on the layered structure stability at both low and high potentials.[136–140] To determine how vacancies improve the structural stability, Yang *et al.*[128] investigated structural and electrochemical behavior changes by designing vacancy-containing P2-type $Na_{2/3}[Zn_{1/9}Mn_{7/9}\square_{1/9}]O_2$ (NZMO-Vac; with vacancies in the TM layer). The low-spin Mn^{3+} ion content increased after the introduction of vacancies at a low voltage, which was ascribed to the shortened Mn–O bond, as shown in (Fig. 10a). It is well known that high-spin Mn^{3+} ions are the main reason for the undesirable structural degradation and substantial capacity fading of MLO materials. Thus, increasing the content of low-spin Mn^{3+} is key to avoiding J–T distortion. Fig. 10b shows the coexistence of 23.6% low-spin Mn^{3+} and 10.9% high-spin Mn^{3+} ions in the discharged NZMO-Vac. Meanwhile, the oxygen atoms around the formed

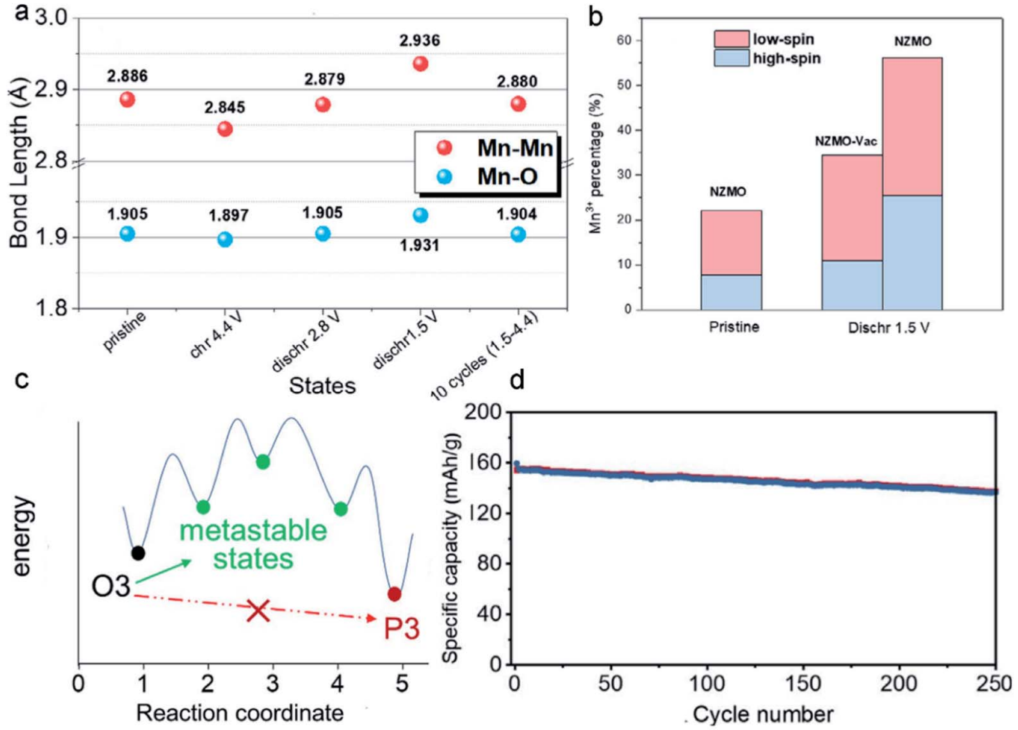

Fig. 10 (a) The evolution of bond lengths in the electrochemical processes. (b) The percentages of the low-spin and high-spin Mn^{3+} ions. Reproduced with permission.[128] Copyright 2021 Elsevier. (c) Schematic illustration of the mechanism behind the prevention of the O3–P3 biphasic reaction. (d) Cycling performance of $Li_{1.2}[Mn_{0.66}Co_{0.17}Ni_{0.17}]_{0.8}O_2$ at 125 mA g^{-1}. Reproduced with permission.[129] Copyright 2021 Wiley-VCH.

vacancies contributed much more charge compensation than those around Zn, accelerating the oxygen redox reaction and enhancing the reversibility of the anionic reaction. In addition, Mn vacancies can provide more ion intercalation sites, giving rise to reduced charge transfer resistance and improved specific capacitance. Correspondingly, NZMO-Vac delivered a much higher capacity than NZMO (204 and 187 mA h g^{-1} for NZMO-Vac and NZMO, respectively) at 0.02 A g^{-1} in the first cycle. Moreover, the NZMO-Vac retained 43.4% capacity after 100 cycles, which is better than the 25.6% of NZMO.

In addition to single vacancies, the introduction of mixed vacancies is also an effective way to suppress structural degradation due to the synergistic effects between anionic and cationic vacancies. In both P2-type and O3-type MLO materials, the irreversible layer gliding causes huge volume changes and significantly jeopardizes the structural stability.[141,142] To solve this problem, reducing the net charge of the oxygen (*i.e.*, creating oxygen vacancies) or enabling reversible TM migration during the charging/discharging process is critical. "Reversible" migration implies that TM can move between the TM layer and alkaline layer but does not need to return to the same site each time. Therefore, cationic vacancies can provide many more sites for TM migration. To demonstrate this concept, Xiao *et al.*[129] prepared an Li- and Mn- rich layered cathode material, in which the formation of oxygen vacancies and Mn vacancies was simultaneous. The results of a combination of computational simulations and systematic characterizations demonstrated that the mixed vacancies enabled the TM to migrate to the tetrahedral sites of the Na layer during desodiation and move back during sodiation. The TM migration suppressed a complete O3–P3 phase transition by increasing the energy barriers and stabilized the performance. Fig. 10c shows the proposed energy evolution during the O3–P3 two-phase reaction by manipulating TM migrations. Such metastable states can immobilize the structure and inhibit the transition to global P stacking. Correspondingly, the Li- and Mn-rich layered cathode material delivered 86% capacity retention after 250 cycles (Fig. 10d). In addition, although the interlayer spacing decreased to 5.0 Å, the diffusion kinetics of Na^+ ions was not affected, which was attributed to the formation of oxygen vacancies and the distortion of the metal oxide layer.

As described above, the incorporation of Mn and/or O ion vacancies in MLO materials promotes ion-reduction/oxidation and bond length changes, which significantly increase the percentage of low-spin Mn^{3+} and provide more sites for the reversible migration of Mn ions. It should be noted that the introduction of vacancies can alter the electronic structure and bonding energy in MLO materials. Too high amount of vacancies may sacrifice the conductivity of materials and structural stability. However, how to achieve precise and optimum vacancy concentration is a critical issue in the current synthesis process. Correspondingly, developing new synthesis methods to accurately control the vacancy concentration is necessary. Furthermore, advanced characterization methods to monitor the generation process of vacancies are also needed.

4.4 Novel structural design

Structural stability during the electrochemical reaction is an indispensable requirement of MLO materials. Both O3-type and P2-type Na_xMnO_2 undergo the gliding of oxygen layers during the electrochemical process and suffer from J–T distortion, leading to structural deterioration and undesirable performance. Birnessite-$Na_xMnO_2 \cdot nH_2O$ possesses a much larger interlayer spacing (~7 Å) than the O2 (~5 Å) and P3 (~5 Å) phase, increasing the rate of Na^+ diffusion. In contrast, no oxygen layer gliding occurs in Birnessite-$Na_xMnO_2 \cdot nH_2O$ during oxidation due to the pillar effect of crystal water; the corresponding layered structure can offer protection against J–T distortion and structural degradation.[143,144] Nevertheless, it should be taken into account that crystal water in the interlayer may limit Na accommodation and hinder Na^+ diffusion. Meanwhile, crystal water is extracted in the oxidation process, and the presence of water in the electrolyte greatly impacts its stability and accelerates decomposition.

To address these issues, Xia *et al.* designed a novel monoclinic polymorph $NaMnO_{2-y-\delta}(OH)_{2y}$ with the coexistence of the O′3 and H′3.[47] In sharp contrast to the monoclinic, O3-, and P2-Na_xMnO_2, the monoclinic polymorph $NaMnO_{2-y-\delta}(OH)_{2y}$ has a larger interlayer distance (~7 Å), which greatly enhances the kinetics of Na^+ ion diffusion. The large interlayer space is attributed to the simultaneous formation of O′3 and H′3 phases with six-coordinate octahedral sites and eight-coordinate hexahedral sites, respectively. It was found that the generated O vacancy in this material can reduce the bandgap, suggesting the enhanced electronic conductivity of $NaMnO_{2-y-\delta}(OH)_{2y}$. Therefore, $NaMnO_{2-y-\delta}(OH)_{2y}$ with large interlayered spacing and high electronic conductivity accelerates the electron and ion transport in the electrode, which enables the $NaMnO_{2-y-\delta}(OH)_{2y}$ electrode to maintain a large capacity of 156 mA h g^{-1} even at the current density of 50C, outperforming the previously reported data in this field. In addition, the reduced distortion of Mn–O and the small β angle in $NaMnO_{2-y-\delta}(OH)_{2y}$ are beneficial to suppress the J–T distortion and minimize the volume change during electrochemical processes (Fig. 11a). These attributes explain why $NaMnO_{2-y-\delta}(OH)_{2y}$ can achieve superior structural stability and excellent cycle performance. As a result,

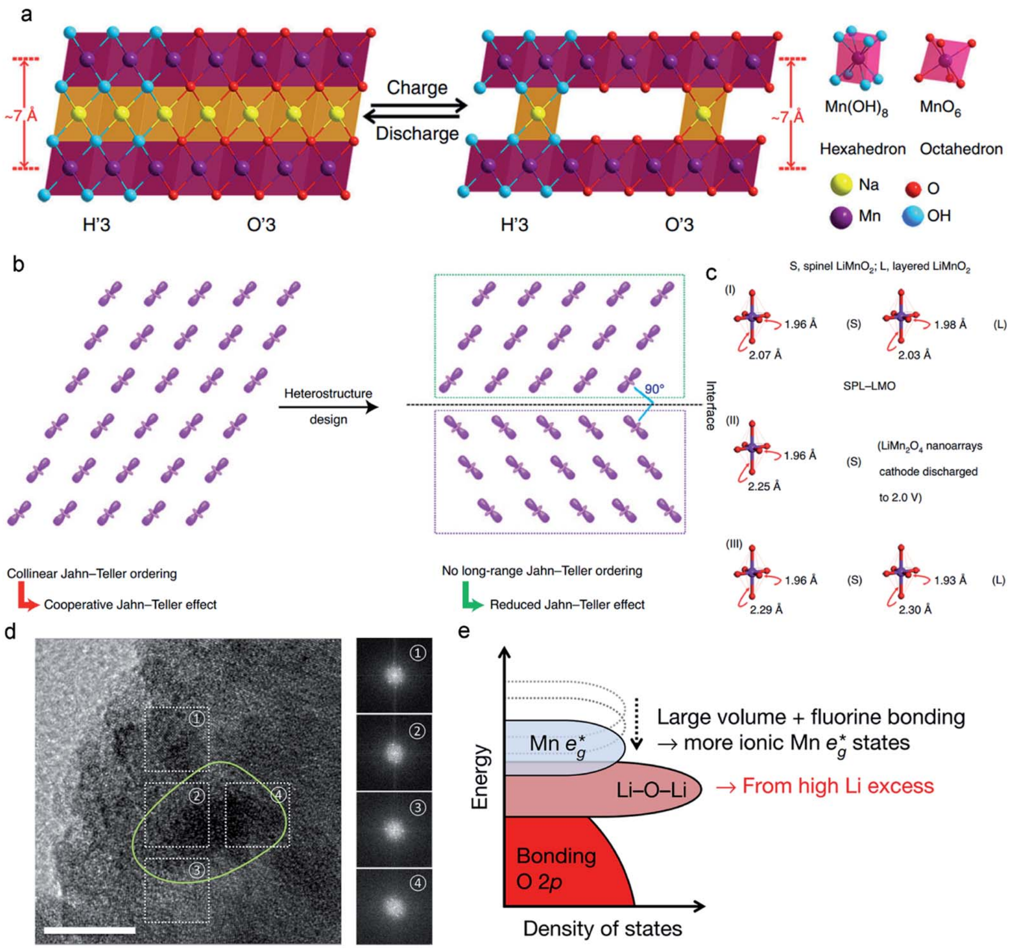

Fig. 11 (a) Reversible crystal structure change of the monoclinic H′3/O′3 $NaMnO_{2-y-\delta}(OH)_{2y}$ in the electrochemical processes. Reproduced with permission.[47] Copyright 2018 Springer Nature. (b) Alleviating Jahn–Teller distortion by interfacial structure manipulation in spinel–layered $LiMnO_2$. (c) Bond lengths of MnO_6 octahedra in spinel–layered $LiMnO_2$, spinel $LiMnO_2$, and monoclinic $LiMnO_2$. Reproduced with permission.[44] Copyright 2021 Springer Nature. (d) A high-magnification TEM image of polycrystalline $Li_2Mn_{2/3}Nb_{1/3}O_2F$ (yellow circle). Reproduced with permission.[130] Copyright 2018 Springer Nature.

the prepared $NaMnO_{2-y-\delta}(OH)_{2y}$ electrode achieved outstanding cycling stability (94.6% capacity retention at 10C over 1000 cycles) than the Birnessite $NaMnO_{2-y-\delta}(OH)_{2y}\cdot 0.61H_2O$ (78% capacity retention at 10C over 1000 cycles).

Designing novel interface structures is also effective in suppressing J–T distortion. Considering the orbital ordering in Mn^{3+}-containing MLO materials, such as $LiMnO_2$, which can generate the collinear J–T order, the strong cooperative J–T effect may cause a large volume change and promote structural degradation (Fig. 11b). To eliminate this cooperative J–T effect, Xia *et al.*[44] designed a unique heterostructure of $LiMnO_2$. The heterostructure comprised layered and spinel domains with various orientations for J–T distortion, which can effectively disrupt the long-range collinear J–T ordering for either the spinel phase or the layered phase in the heterostructure. Fig. 11c compares the axial Mn–O bond elongation in this heterostructure with those in spinel and monoclinic $LiMnO_2$. The heterostructure increased the axial Mn–O bonds from 1.96 to 2.07 Å in spinel $LiMnO_2$ and 1.98 to 2.03 Å in monoclinic $LiMnO_2$, which corresponds to 5.5% and 2.5% distorted degrees, respectively. For layered $LiMnO_2$ and spinel $Li_2Mn_2O_4$,[69,145] the distortion degrees were 18.0% and 15.9%, respectively, much higher than the corresponding phase in the heterostructure. Therefore, the layered–spinel heterostructure with controlled interfacial orbital ordering significantly suppressed J–T distortion. The electrochemical results demonstrated that the $LiMnO_2$ heterostructure cathode delivered high specific capability $\sim$254.3 mA h g^{-1} with 97% coulombic efficiency. Furthermore, such a heterostructure achieved a high specific capacity of 183.6 mA h g^{-1} at 12C. Unprecedented cycling stability with $\sim$90.4% capacity retention over 2000 cycles was achieved, demonstrating the significant effect of interfacial engineering on mitigating J–T distortion.

Cation-disordered lithium-rich MLO materials are another example of a novel structure.[146] Lee *et al.*[130] prepared a new cation-disordered (disordered rock-salt structure) material $Li_2Mn_{2/3}Nb_{1/3}O_2F$ by manipulating the layered phase of Li_2MnO_3 (Fig. 11d). The disordered rock-salt structure, originating from a layered structure, can generate more 0 TM channels.[147] This diffusion channel has a low migration barrier, giving rise to fast Li^+ diffusion kinetics. Furthermore, with cation and anion substitution, the disordered rock-salt Li-rich cathodes could deliver a high capacity (>300 mA h g^{-1}), mainly from the Mn^{2+}/Mn^{4+} double electron reaction (Fig. 11e). This Mn^{2+}/Mn^{4+} double redox effectively suppresses the problems associated with O redox by reducing the anionic redox reaction content.

In short, novel structural design shows notable effectiveness in manipulating the localized structure to suppress the J–T effect, providing stable units in localized regions and thus effectively eliminating electrochemical degradation. Nevertheless, novel structural design faces great challenges, countering which needs an in-depth understanding of the structure–property relationships in MLO materials. Additionally, accurately manipulating the structure at the atomic level is difficult, which is not suited to large-scale applications in most cases.

5. Conclusion and future perspectives

In recent decades, endeavors to build a holistic understanding of the impact of electrochemistry on the structural degradation of MLO materials have experienced a revival. Substantial progress has been made in the field of MLO materials for various energy storage technologies. All in all, developing MLO materials with high capacity, high voltage, high stability, and high rate in energy storage is our target. To reach this target, the irreversible phase transformation, Mn dissolution/disproportionation reaction, interfacial degradation arising from Mn^{2+}, and crack formation induced by J–T distortion must be better understood at the atomic level. From the perspective of structure–property relationships in MLO materials, this review comprehensively summarizes structure and property optimization for high-efficiency energy storage. First, elemental doping can restrain the elongated bonds and stabilize the metastable structure to inhibit J–T distortion during the electrochemical process, preventing structural degradation. Second, the interlayer structure can be manipulated by pre-intercalating ions or molecules, which serve as pillars against lattice change and endow MLO materials with a robust layered structure and/or large interlayer spacing to accommodate J–T distortion, resulting in fast diffusion kinetics and high cycling stability. Third, the incorporation of Mn and/or O ion vacancies in MLO materials promotes ion-reduction/oxidation and bond length changes, which significantly increase the percentage of low-spin Mn^{3+} and provide more sites for the reversible migration of Mn ions. Finally, novel structural design shows notable effectiveness in manipulating the localized structure to suppress the J–T effect, providing stable units in localized regions and thus effectively eliminating electrochemical degradation.

Although various strategies have paved effective pathways to suppress electrochemical degradation, it is still difficult to thoroughly disentangle the issues raised above. Additional research efforts are needed to develop methods for stabilizing the crystal structure during electrochemical processes to suppress capacity degradation in the representative MLO systems. Our suggestions are as follows:

(1) Coupling various strategies to induce synergistic effects for high-performance MLO materials. Each strategy may have a limited effect on suppressing the degradation of MLO cathodes. In this case, integrating various strategies to exploit their synergistic effects may be worth exploring. For example, combining doping and interlayer manipulation may realize robust structural stability and fast diffusion kinetics.

(2) Developing novel MLO materials with stable structures. Presently, most MLO materials still have structural issues and are sensitive to air containing water vapor. It is critically necessary to innovate MLO materials with highly stable localized structures and microstructures by modulating the electronic states and tailoring the crystal domains. In addition, advanced machine learning and theoretical calculations can be applied to design and develop high-performance MLO

materials. With improved computational analyses, it is possible to gain some quantitative comprehension of the effect of each adverse factor on structural stability using qualitative constraints in simulations.

(3) Realizing accurate MLO cathode characterization and comprehensively elucidating the structure–property correlations. Electrochemical energy storage devices store energy through electrochemical reactions. However, the understanding of the intrinsic electrochemical reaction mechanisms in MLO materials is still limited due to the complexity of each energy storage system and the effects of electrolytes, conductive carbon additives, and binders. In this regard, powerful characterization techniques, such as *in situ* transmission electron microscopy, *in situ* X-ray absorption spectroscopy, and electrochemical quartz crystal microbalance analysis, are indispensable to distinguish the dynamic structural evolution and electrochemical behaviors of MLO cathodes and comprehensively understand their structure–property correlations.

In conclusion, a comprehensive understanding of the electrochemical degradation mechanisms at the atomic level is essential for developing high-performance MLO cathodes, as is systematically outlined in this review. Although numerous challenges remain, the future is bright thanks to the tremendous endeavors to elucidate J–T distortion and the continual development of effective strategies, advanced characterization techniques, artificial intelligence, and theoretical calculations. We hope that the synergistic application of experiments and computational modeling will dramatically improve our understanding of the chemical degradation mechanisms and the electrochemical performance of energy storage systems based on MLO cathodes.

Conflicts of interest

The authors declare no conflict of interest.

Acknowledgements

T. Z. and H. X. acknowledge the support from the National Natural Science Foundation of China (No. 52072179, 52061135201, 51772154, and 51972174), Natural Science Foundation of Jiangsu Province (No. BK20200073), and the Fundamental Research Funds for the Central Universities (No. 30919011108 and 30920041118).

References

1 G. Harper, R. Sommerville, E. Kendrick, L. Driscoll, P. Slater, R. Stolkin, A. Walton, P. Christensen, O. Heidrich and S. Lambert, *Nature*, 2019, **575**, 75–86.
2 P. P. Lopes and V. R. Stamenkovic, *Science*, 2020, **369**, 923–924.
3 X. Chen, X. Shen, T. Z. Hou, R. Zhang, H. J. Peng and Q. Zhang, *Chem*, 2020, **6**, 2242–2256.
4 S. Sun, C. Z. Zhao, H. Yuan, Y. Lu, J. K. Hu, J. Q. Huang and Q. Zhang, *Mater. Futures*, 2021, **1**, 012101.
5 Y. Lu, C. Z. Zhao, R. Zhang, H. Yuan, L. P. Hou, Z. H. Fu, X. Chen, J. Q. Huang and Q. Zhang, *Sci. Adv.*, 2021, **7**, eabi5520.
6 Q. Guo, S. Sun, K. i. Kim, H. Zhang, X. Liu, C. Yan and H. Xia, *Carbon Energy*, 2021, **3**, 440–448.
7 S. Sun, B. Liu, H. Zhang, Q. Guo, Q. Xia, T. Zhai and H. Xia, *Adv. Energy Mater.*, 2021, **11**, 2003599.
8 Q. Xia, Q. Zhang, S. Sun, F. Hussain, C. Zhang, X. Zhu, F. Meng, K. Liu, H. Geng and J. Xu, *Adv. Mater.*, 2021, **33**, 2003524.
9 Q. Guo, K. I. Kim, S. Li, A. M. Scida, P. Yu, S. K. Sandstrom, L. Zhang, S. Sun, H. Jiang and Q. Ni, *ACS Energy Lett.*, 2021, **6**, 459–467.
10 S. Sun, D. Rao, T. Zhai, Q. Liu, H. Huang, B. Liu, H. Zhang, L. Xue and H. Xia, *Adv. Mater.*, 2020, **32**, 2005344.
11 M. Jiang, D. L. Danilov, R. A. Eichel and P. H. Notten, *Adv. Energy Mater.*, 2021, **11**, 2103005.
12 M. H. Han, E. Gonzalo, G. Singh and T. Rojo, *Energy Environ. Sci.*, 2015, **8**, 81–102.
13 L. Xue, S. Li, T. Shen, M. Ni, C. Qiu, S. Sun, H. Geng, X. Zhu and H. Xia, *Energy Storage Mater.*, 2020, **32**, 272–280.
14 C. Grey and J. Tarascon, *Nat. Mater.*, 2017, **16**, 45–56.
15 L. Fang, J. Xu, S. Sun, B. Lin, Q. Guo, D. Luo and H. Xia, *Small*, 2019, **15**, 1804806.
16 Q. Xia, S. Sun, J. Xu, F. Zan, J. Yue, Q. Zhang, L. Gu and H. Xia, *Small*, 2018, **14**, 1804149.
17 M. Dixit, B. Markovsky, F. Schipper, D. Aurbach and D. T. Major, *J. Phys. Chem. C*, 2017, **121**, 22628–22636.
18 X. Shan, F. Guo, D. S. Charles, Z. Lebens-Higgins, S. Abdel Razek, J. Wu, W. Xu, W. Yang, K. L. Page and J. C. Neuefeind, *Nat. Commun.*, 2019, **10**, 4975.
19 S. Boyd, K. Ganeshan, W. Y. Tsai, T. Wu, S. Saeed, D. e. Jiang, N. Balke, A. C. van Duin and V. Augustyn, *Nat. Mater.*, 2021, **20**, 1689–1694.
20 R. Jia, J. Yue, Q. Xia, J. Xu, X. Zhu, S. Sun, T. Zhai and H. Xia, *Energy Storage Mater.*, 2018, **13**, 303–311.
21 C. Delmas, C. Fouassier and P. Hagenmuller, *Physica B+C*, 1980, **99**, 81–85.
22 X. Cao, Y. Qiao, M. Jia, P. He and H. Zhou, *Adv. Energy Mater.*, 2022, **12**, 2003972.
23 S. Zhu, W. Huo, X. Liu and Y. Zhang, *Nanoscale Adv.*, 2020, **2**, 37–54.
24 B. Lin, X. Zhu, L. Fang, X. Liu, S. Li, T. Zhai, L. Xue, Q. Guo, J. Xu and H. Xia, *Adv. Mater.*, 2019, **31**, 1900060.
25 K. Mizushima, P. Jones, P. Wiseman and J. B. Goodenough, *Mater. Res. Bull.*, 1980, **15**, 783–789.
26 J. Dunitz and L. Orgel, *J. Phys. Chem. Solids*, 1957, **3**, 20–29.
27 M. H. Alfaruqi, J. Gim, S. Kim, J. Song, D. T. Pham, J. Jo, Z. Xiu, V. Mathew and J. Kim, *Electrochem. Commun.*, 2015, **60**, 121–125.
28 Y. Xu, J. Ma, T. Jiang, H. Ding, W. Wang, M. Wang, X. Zheng, J. Sun, Y. Yuan and M. Chuai, *Energy Storage Mater.*, 2022, **47**, 113–121.
29 L. Liu, Y. C. Wu, L. Huang, K. Liu, B. Duployer, P. Rozier, P. L. Taberna and P. Simon, *Adv. Energy Mater.*, 2021, **11**, 2101287.

30 K. W. Nam, S. Kim, S. Lee, M. Salama, I. Shterenberg, Y. Gofer, J. S. Kim, E. Yang, C. S. Park and J. S. Kim, *Nano Lett.*, 2015, **15**, 4071–4079.

31 X. Sun, V. Duffort, B. L. Mehdi, N. D. Browning and L. F. Nazar, *Chem. Mater.*, 2016, **28**, 534–542.

32 H. A. Jahn and E. Teller, *Proc. R. Soc. A: Math. Phys. Eng. Sci.*, 1937, **161**, 220–235.

33 G. Ceder and S. Mishra, *Electrochem. Solid-State*, 1999, **2**, 550.

34 K. Zhang, D. Kim, Z. Hu, M. Park, G. Noh, Y. Yang, J. Zhang, V. W. h. Lau, S. L. Chou and M. Cho, *Nat. Commun.*, 2019, **10**, 5203.

35 M. D. Radin and A. Van der Ven, *Chem. Mater.*, 2018, **30**, 607–618.

36 C. Wang, L. Liu, S. Zhao, Y. Liu, Y. Yang, H. Yu, S. Lee, G. H. Lee, Y. M. Kang and R. Liu, *Nat. Commun.*, 2021, **12**, 2256.

37 W. Zuo, X. Liu, J. Qiu, D. Zhang, Z. Xiao, J. Xie, F. Ren, J. Wang, Y. Li and G. F. Ortiz, *Nat. Commun.*, 2021, **12**, 4903.

38 Y. S. Xu, Y. N. Zhou, Q. H. Zhang, M. Y. Qi, S. J. Guo, J. M. Luo, Y. G. Sun, L. Gu, A. M. Cao and L. J. Wan, *Chem. Eng. J.*, 2021, **412**, 128735.

39 K. Lei, Z. Zhu, Z. Yin, P. Yan, F. Li and J. Chen, *Chem*, 2019, **5**, 3220–3231.

40 P. Yan, J. Zheng, Z. K. Tang, A. Devaraj, G. Chen, K. Amine, J. G. Zhang, L. M. Liu and C. Wang, *Nat. Nanotechnol.*, 2019, **14**, 602–608.

41 Q. Zhao, A. Song, S. Ding, R. Qin, Y. Cui, S. Li and F. Pan, *Adv. Mater.*, 2020, **32**, 2002450.

42 Q. Guo, S. Li, X. Liu, H. Lu, X. Chang, H. Zhang, X. Zhu, Q. Xia, C. Yan and H. Xia, *Adv. Sci.*, 2020, **7**, 1903246.

43 H. Li, W. Zhang, K. Sun, J. Guo, K. Yuan, J. Fu, T. Zhang, X. Zhang, H. Long and Z. Zhang, *Adv. Energy Mater.*, 2021, **11**, 2100867.

44 X. Zhu, F. Meng, Q. Zhang, L. Xue, H. Zhu, S. Lan, Q. Liu, J. Zhao, Y. Zhuang and Q. Guo, *Nat. Sustain.*, 2021, **4**, 392–401.

45 Z. Lu and J. Dahn, *J. Electrochem. Soc.*, 2001, **148**, A237.

46 Y. Zuo, B. Li, N. Jiang, W. Chu, H. Zhang, R. Zou and D. Xia, *Adv. Mater.*, 2018, **30**, 1707255.

47 H. Xia, X. Zhu, J. Liu, Q. Liu, S. Lan, Q. Zhang, X. Liu, J. K. Seo, T. Chen and L. Gu, *Nat. Commun.*, 2018, **9**, 5100.

48 X. Ma, H. Chen and G. Ceder, *J. Electrochem. Soc.*, 2011, **158**, A1307.

49 Y. Zhang, X. Cui, Y. Liu, S. Cheng, P. Cui, Y. Wu, Z. Sun, Z. Shao, J. Fu and E. Xie, *J. Energy Chem.*, 2022, **67**, 225–232.

50 Z. Shi, J. Wu, M. Ni, Q. Guo, F. Zan and H. Xia, *Mater. Res. Bull.*, 2021, **144**, 111475.

51 Z. Shi, L. Xue, J. Wu, Q. Guo, Q. Xia, M. Ni, P. Wang, S. V. Savilov, S. M. Aldoshin and F. Zan, *J. Electrochem. Soc.*, 2021, **168**, 120549.

52 M. Wang and S. Yagi, *J. Alloys Compd.*, 2020, **820**, 153135.

53 P. Almodóvar, D. A. Giraldo, J. Chancón, I. Álvarez-Serrano and M. L. López, *ChemElectroChem*, 2020, **7**, 2102–2106.

54 S. Chong, Y. Wu, C. Liu, Y. Chen, S. Guo, Y. Liu and G. Cao, *Nano Energy*, 2018, **54**, 106–115.

55 J. Billaud, R. J. Clément, A. R. Armstrong, J. Canales-Vázquez, P. Rozier, C. P. Grey and P. G. Bruce, *J. Am. Chem. Soc.*, 2014, **136**, 17243–17248.

56 D. H. Seo, J. Lee, A. Urban, R. Malik, S. Kang and G. Ceder, *Nat. Chem.*, 2016, **8**, 692–697.

57 M. D. Radin, J. Vinckeviciute, R. Seshadri and A. van der Ven, *Nat. Energy*, 2019, **4**, 639–646.

58 J. Wang, J. G. Wang, H. Liu, C. Wei and F. Kang, *J. Mater. Chem. A*, 2019, **7**, 13727–13735.

59 C. Costentin, T. R. Porter and J. M. Savéant, *ACS Appl. Mater. Interfaces*, 2017, **9**, 8649–8658.

60 W. Wei, X. Cui, W. Chen and D. G. Ivey, *Chem. Soc. Rev.*, 2011, **40**, 1697–1721.

61 M. Mateos, N. Makivic, Y. s. Kim, B. Limoges and V. Balland, *Adv. Energy Mater.*, 2020, **10**, 2000332.

62 L. Liu, L. Su, Y. Lu, Q. Zhang, L. Zhang, S. Lei, S. Shi, M. D. Levi and X. Yan, *Adv. Funct. Mater.*, 2019, **29**, 1806778.

63 G. Vitins and K. West, *J. Electrochem. Soc.*, 1997, **144**, 2587.

64 M. Tabuchi, K. Ado, H. Kobayashi, H. Kageyama, C. Masquelier, A. Kondo and R. Kanno, *J. Electrochem. Soc.*, 1998, **145**, L49.

65 S. J. Hwang, H. S. Park, J. H. Choy and G. Campet, *Chem. Mater.*, 2000, **12**, 1818–1826.

66 J. Paulsen, C. Thomas and J. Dahn, *J. Electrochem. Soc.*, 1999, **146**, 3560.

67 Q. Chen, S. Sun, T. Zhai, M. Yang, X. Zhao and H. Xia, *Adv. Energy Mater.*, 2018, **8**, 1800054.

68 J. Reimers, E. W. Fuller, E. Rossen and J. Dahn, *J. Electrochem. Soc.*, 1993, **140**, 3396.

69 A. R. Armstrong and P. G. Bruce, *Nature*, 1996, **381**, 499–500.

70 C. Delmas, D. Carlier and M. Guignard, *Adv. Energy Mater.*, 2021, **11**, 2001201.

71 H. Ji, J. Wu, Z. Cai, J. Liu, D. H. Kwon, H. Kim, A. Urban, J. K. Papp, E. Foley and Y. Tian, *Nat. Energy*, 2020, **5**, 213–221.

72 C. Zuo, Z. Hu, R. Qi, J. Liu, Z. Li, J. Lu, C. Dong, K. Yang, W. Huang and C. Chen, *Adv. Energy Mater.*, 2020, **10**, 2000363.

73 A. Manthiram, *Nat. Commun.*, 2020, **11**, 1550.

74 A. D. Robertson, A. R. Armstrong and P. G. Bruce, *Chem. Mater.*, 2001, **13**, 2380–2386.

75 A. R. Armstrong, A. D. Robertson, R. Gitzendanner and P. G. Bruce, *J. Solid State Chem.*, 1999, **145**, 549–556.

76 C. Fouassier, G. Matejka, J. M. Reau and P. Hagenmuller, *J. Solid State Chem.*, 1973, **6**, 532–537.

77 A. M. Abakumov, A. A. Tsirlin, I. Bakaimi, G. Van Tendeloo and A. Lappas, *Chem. Mater.*, 2014, **26**, 3306–3315.

78 O. Velikokhatnyi, C. C. Chang and P. Kumta, *J. Electrochem. Soc.*, 2003, **150**, A1262.

79 R. Hoppe, G. Brachtel and M. Jansen, *Z. Anorg. Allg. Chem.*, 1975, **417**, 1–10.

80 X. Chen, Y. Wang, K. Wiaderek, X. Sang, O. Borkiewicz, K. Chapman, J. LeBeau, J. Lynn and X. Li, *Adv. Funct. Mater.*, 2018, **28**, 1805105.

81 X. Li, X. Ma, D. Su, L. Liu, R. Chisnell, S. P. Ong, H. Chen, A. Toumar, J. C. Idrobo and Y. Lei, *Nat. Mater.*, 2014, **13**, 586–592.

82 J. Sun, C. Sheng, X. Cao, P. Wang, P. He, H. Yang, Z. Chang, X. Yue and H. Zhou, *Adv. Funct. Mater.*, 2022, **32**, 2110295.

83 W. E. Gent, K. Lim, Y. Liang, Q. Li, T. Barnes, S. J. Ahn, K. H. Stone, M. McIntire, J. Hong and J. H. Song, *Nat. Commun.*, 2017, **8**, 2091.

84 J. S. Kim, C. S. Johnson, J. T. Vaughey, M. M. Thackeray, S. A. Hackney, W. Yoon and C. P. Grey, *Chem. Mater.*, 2004, **16**, 1996–2006.

85 M. M. Thackeray, S. H. Kang, C. S. Johnson, J. T. Vaughey, R. Benedek and S. Hackney, *J. Mater. Chem.*, 2007, **17**, 3112–3125.

86 G. Assat and J. M. Tarascon, *Nat. Energy*, 2018, **3**, 373–386.

87 D. Eum, B. Kim, S. J. Kim, H. Park, J. Wu, S. P. Cho, G. Yoon, M. H. Lee, S. K. Jung and W. Yang, *Nat. Mater.*, 2020, **19**, 419–427.

88 Q. Chu, X. Wang, X. Zhang, Q. Li and X. Liu, *Inorg. Chem.*, 2011, **50**, 2049–2051.

89 M. Gu, I. Belharouak, J. Zheng, H. Wu, J. Xiao, A. Genc, K. Amine, S. Thevuthasan, D. R. Baer and J. G. Zhang, *ACS Nano*, 2013, **7**, 760–767.

90 P. F. Wang, Y. You, Y. X. Yin and Y. G. Guo, *Adv. Energy Mater.*, 2018, **8**, 1701912.

91 A. Singer, M. Zhang, S. Hy, D. Cela, C. Fang, T. Wynn, B. Qiu, Y. Xia, Z. Liu and A. Ulvestad, *Nat. Energy*, 2018, **3**, 641–647.

92 G. Assat, D. Foix, C. Delacourt, A. Iadecola, R. Dedryvère and J.-M. Tarascon, *Nat. Commun.*, 2017, **8**, 2219.

93 Q. Li, D. Ning, D. Zhou, K. An, D. Wong, L. Zhang, Z. Chen, G. Schuck, C. Schulz and Z. Xu, *J. Mater. Chem. A*, 2020, **8**, 7733–7745.

94 M. Freire, N. V. Kosova, C. Jordy, D. Chateigner, O. Lebedev, A. Maignan and V. Pralong, *Nat. Mater.*, 2016, **15**, 173–177.

95 S. Myeong, W. Cho, W. Jin, J. Hwang, M. Yoon, Y. Yoo, G. Nam, H. Jang, J. G. Han and N. S. Choi, *Nat. Commun.*, 2018, **9**, 3285.

96 P. Liu, H. Zhang, W. He, T. Xiong, Y. Cheng, Q. Xie, Y. Ma, H. Zheng, L. Wang and Z. Z. Zhu, *J. Am. Chem. Soc.*, 2019, **141**, 10876–10882.

97 Y. Koyama, I. Tanaka, M. Nagao and R. Kanno, *J. Power Sources*, 2009, **189**, 798–801.

98 M. H. Alfaruqi, S. Islam, D. Y. Putro, V. Mathew, S. Kim, J. Jo, S. Kim, Y. K. Sun, K. Kim and J. Kim, *Electrochim. Acta*, 2018, **276**, 1–11.

99 Z. Liu, G. Fang, L. Qin, X. Cao, J. Zhou, A. Pan, S. Wang and S. Liang, *Prog. Mater. Sci.*, 2021, 100911.

100 X. Zhao, L. Mao, Q. Cheng, F. Liao, G. Yang, X. Lu and L. Chen, *Energy Storage Mater.*, 2021, **38**, 397–437.

101 J. Huang, Z. Wang, M. Hou, X. Dong, Y. Liu, Y. Wang and Y. Xia, *Nat. Commun.*, 2018, **9**, 2906.

102 B. Song, J. I. Choi, Y. Zhu, Z. Geng, L. Zhang, Z. Lin, C. c. Tuan, K.-s. Moon and C. p. Wong, *Chem. Mater.*, 2016, **28**, 9110–9121.

103 H. Y. Asl and A. Manthiram, *Science*, 2020, **369**, 140–141.

104 C. Wang, L. Xing, J. Vatamanu, Z. Chen, G. Lan, W. Li and K. Xu, *Nat. Commun.*, 2019, **10**, 3423.

105 J. Yang, S. Muhammad, M. R. Jo, H. Kim, K. Song, D. A. Agyeman, Y. I. Kim, W. S. Yoon and Y. M. Kang, *Chem. Soc. Rev.*, 2016, **45**, 5717–5770.

106 A. R. Armstrong, N. Dupre, A. J. Paterson, C. P. Grey and P. G. Bruce, *Chem. Mater.*, 2004, **16**, 3106–3118.

107 M. R. Jo, Y. Kim, J. Yang, M. Jeong, K. Song, Y. I. Kim, J. M. Lim, M. Cho, J. H. Shim and Y. M. Kim, *Nat. Commun.*, 2019, **10**, 3385.

108 J. Reed, G. Ceder and A. van der Ven, *Electrochem. Solid-State*, 2001, **4**, A78.

109 J. Reed and G. Ceder, *Chem. Rev.*, 2004, **104**, 4513–4534.

110 S. Sharifi-Asl, V. Yurkiv, A. Gutierrez, M. Cheng, M. Balasubramanian, F. Mashayek, J. Croy and R. Shahbazian-Yassar, *Nano Lett.*, 2019, **20**, 1208–1217.

111 C. Zhan, T. Wu, J. Lu and K. Amine, *Energy Environ. Sci.*, 2018, **11**, 243–257.

112 N. Kumagai, S. Komaba, Y. Kataoka and M. Koyanagi, *Chem. Lett.*, 2000, **29**, 1154–1155.

113 C. Delacourt, A. Kwong, X. Liu, R. Qiao, W. Yang, P. Lu, S. Harris and V. Srinivasan, *J. Electrochem. Soc.*, 2013, **160**, A1099.

114 S. Komaba, N. Kumagai and Y. Kataoka, *Electrochim. Acta*, 2002, **47**, 1229–1239.

115 J. Wandt, A. Freiberg, R. Thomas, Y. Gorlin, A. Siebel, R. Jung, H. A. Gasteiger and M. Tromp, *J. Mater. Chem. A*, 2016, **4**, 18300–18305.

116 X. Xiao, Z. Liu, L. Baggetto, G. M. Veith, K. L. More and R. R. Unocic, *Phys. Chem. Chem. Phys.*, 2014, **16**, 10398–10402.

117 P. Yan, J. Zheng, M. Gu, J. Xiao, J. G. Zhang and C. M. Wang, *Nat. Commun.*, 2017, **8**, 14101.

118 C. J. Chen, W. K. Pang, T. Mori, V. K. Peterson, N. Sharma, P.-H. Lee, S. h. Wu, C. C. Wang, Y. F. Song and R. S. Liu, *J. Am. Chem. Soc.*, 2016, **138**, 8824–8833.

119 P. Yan, J. Zheng, J. Zheng, Z. Wang, G. Teng, S. Kuppan, J. Xiao, G. Chen, F. Pan and J. G. Zhang, *Adv. Energy Mater.*, 2016, **6**, 1502455.

120 F. Lin, I. M. Markus, D. Nordlund, T. C. Weng, M. D. Asta, H. L. Xin and M. M. Doeff, *Nat. Commun.*, 2014, **5**, 3529.

121 X. Cui, S. Wang, X. Ye, X. Fan, C. Gao, Y. Quan, S. Wen, X. Cai, J. Huang and S. Li, *Energy Storage Mater.*, 2022, **45**, 1153–1164.

122 S. Zhou, G. Wang, W. Tang, Y. Xiao and K. Yan, *Electrochim. Acta*, 2018, **261**, 565–577.

123 H. Zhu, Q. Li, X. Gong, K. Cao and Z. Chen, *Crystals*, 2018, **8**, 425.

124 Y. Zhao, Q. Fang, X. Zhu, L. Xue, M. Ni, C. Qiu, H. Huang, S. Sun, S. Li and H. Xia, *J. Mater. Chem. A*, 2020, **8**, 8969–8978.

125 Y. Wang, X. Wang, X. Li, R. Yu, M. Chen, K. Tang and X. Zhang, *Chem. Eng. J.*, 2019, **360**, 139–147.

126 N. Jabeen, A. Hussain, Q. Xia, S. Sun, J. Zhu and H. Xia, *Adv. Mater.*, 2017, **29**, 1700804.

127 S. Chu, C. Zhang, H. Xu, S. Guo, P. Wang and H. Zhou, *Angew. Chem., Int. Ed.*, 2021, **133**, 13478–13483.

128 L. Yang, Z. Liu, X. Shen, S. Li, Z. Hu, Q. Kong, J. Ma, J. Li, H.-J. Lin and C. T. Chen, *Energy Storage Mater.*, 2022, **44**, 231–238.

129 B. Xiao, Y. Wang, S. Tan, M. Song, X. Li, Y. Zhang, F. Lin, K. S. Han, F. Omenya and K. Amine, *Angew. Chem., Int. Ed.*, 2021, **60**, 8258–8267.

130 J. Lee, D. A. Kitchaev, D. H. Kwon, C. W. Lee, J. K. Papp, Y. S. Liu, Z. Lun, R. J. Clement, T. Shi and B. D. McCloskey, *Nature*, 2018, **556**, 185–190.

131 Q. Chen, Y. Pei, H. Chen, Y. Song, L. Zhen, C. Y. Xu, P. Xiao and G. Henkelman, *Nat. Commun.*, 2020, **11**, 3411.

132 D. Kim, J. M. Lim, M. S. Park, K. Cho and M. Cho, *ACS Appl. Mater. Interfaces*, 2016, **8**, 16631–16639.

133 N. Jabeen, Q. Xia, S. V. Savilov, S. M. Aldoshin, Y. Yu and H. Xia, *ACS Appl. Mater. Interfaces*, 2016, **8**, 33732–33740.

134 N. Zhang, F. Cheng, J. Liu, L. Wang, X. Long, X. Liu, F. Li and J. Chen, *Nat. Commun.*, 2017, **8**, 405.

135 H. Pan, Y. Shao, P. Yan, Y. Cheng, K. S. Han, Z. Nie, C. Wang, J. Yang, X. Li and P. Bhattacharya, *Nat. Energy*, 2016, **1**, 16039.

136 Y. Li, X. Wang, Y. Gao, Q. Zhang, G. Tan, Q. Kong, S. Bak, G. Lu, X. Q. Yang and L. Gu, *Adv. Energy Mater.*, 2019, **9**, 1803087.

137 B. Song, M. Tang, E. Hu, O. J. Borkiewicz, K. M. Wiaderek, Y. Zhang, N. D. Phillip, X. Liu, Z. Shadike and C. Li, *Chem. Mater.*, 2019, **31**, 3756–3765.

138 B. Liu, S. Sun, R. Jia, H. Zhang, X. Zhu, C. Zhang, J. Xu, T. Zhai and H. Xia, *Adv. Funct. Mater.*, 2020, **30**, 1909546.

139 S. Sun, Q. Xia, J. Liu, J. Xu, F. Zan, J. Yue, S. V. Savilov, V. V. Lunin and H. Xia, *J. Materiomics*, 2019, **5**, 229–236.

140 T. Zhai, S. Sun, X. Liu, C. Liang, G. Wang and H. Xia, *Adv. Mater.*, 2018, **30**, 1706640.

141 N. Yabuuchi, K. Kubota, M. Dahbi and S. Komaba, *Chem. Rev.*, 2014, **114**, 11636–11682.

142 S. She, Y. Zhu, Y. Chen, Q. Lu, W. Zhou and Z. Shao, *Adv. Energy Mater.*, 2019, **9**, 1900429.

143 K. W. Nam, S. Kim, E. Yang, Y. Jung, E. Levi, D. Aurbach and J. W. Choi, *Chem. Mater.*, 2015, **27**, 3721–3725.

144 S. Sun, T. Zhai, C. Liang, S. V. Savilov and H. Xia, *Nano Energy*, 2018, **45**, 390–397.

145 A. Mosbah, A. Verbaere and M. Tournoux, *Mater. Res. Bull.*, 1983, **18**, 1375–1381.

146 Q. Zhang, C. Didier, W. K. Pang, Y. Liu, Z. Wang, S. Li, V. K. Peterson, J. Mao and Z. Guo, *Adv. Energy Mater.*, 2019, **9**, 1900568.

147 J. Lee, A. Urban, X. Li, D. Su, G. Hautier and G. Ceder, *Science*, 2014, **343**, 519–522.